OKLAHOMA TRANSPORTATION CENTER

ECONOMIC ENHANCEMENT THROUGH INFRASTRUCTURE STEWARDSHIP

STRUCTURAL IDENTIFICATION OF A REAL-WORLD SHEAR-CRITICAL PRESTRESSED CONCRETE HIGHWAY BRIDGE

PENG F. TANG
JIN-SONG PEI, PH.D.
ANDREW W. SMYTH, PH.D.
LUTHER W. WHITE, PH.D.

OTCREOS9.1-36-F

Oklahoma Transportation Center
2601 Liberty Parkway, Suite 110
Midwest City, Oklahoma 73110

Phone: 405.732.6580
Fax: 405.732.6586
www.oktc.org

DISCLAIMER

TECHNICAL REPORT DOCUMENTATION PAGE

1. REPORT NO. OTCREOS9.1-36-F	2. GOVERNMENT ACCESSION NO.	3. RECIPIENTS CATALOG NO.
4. TITLE AND SUBTITLE Structural Identification of a Real-World Shear-Critical Prestressed Concrete Highway Bridge		5. REPORT DATE August 31, 2012 6. PERFORMING ORGANIZATION CODE
7. AUTHOR(S) Peng F. Tang, Jin-Song Pei, Andrew W. Smyth, and Luther W. White		8. PERFORMING ORGANIZATION REPORT
9. PERFORMING ORGANIZATION NAME AND ADDRESS School of Civil Engineering and Environmental Science The University of Oklahoma 202 W. Boyd, Rm 334 Norman, Oklahoma 73019		10. WORK UNIT NO. 11. CONTRACT OR GRANT NO. DTRT06-G-0016
12. SPONSORING AGENCY NAME AND ADDRESS Oklahoma Transportation Center (Fiscal) 201 ATRC Stillwater, OK 74078 (Technical) 2601 Liberty Parkway, Suite 110 Midwest City, OK 73110		13. TYPE OF REPORT AND PERIOD COVERED Final June 2009- August 2012 14. SPONSORING AGENCY CODE
15. SUPPLEMENTARY NOTES University Transportation Center		

16. ABSTRACT

A typical span of the Little River overflow bridge located in McCurtain County, Oklahoma, a shear-critical prestressed concrete bridge identified by the Oklahoma Department of Transportation (ODOT) Bridge Division, is studied using a multidisciplinary approach. Field measurements are collected in terms of accelerations. They are processed in both time-domain and frequency-domain analyses. The results are validated and interpreted using the principles in structural engineering to reveal the insights about the bridge span; new findings are discovered and reported to the ODOT Bridge Division. These findings and our developed systematic approach will be widely disseminated in the ASCE structural health monitoring community given the inherent challenge in processing and understanding dynamic measurements of real-world structures. These data processing and result analysis efforts are the focus of this report, while snapshots of our other work, including finite element modeling of the bridge span, nonlinear system identification and model updating, are provided.

17. KEY WORDS structural health monitoring, prestressed concrete bridge, ambient vibrations, vibration-based methods, frequency-domain analysis, nonstationarity of data.	18. DISTRIBUTION STATEMENT No restrictions. This publication is available at www.oktc.org and from the NTIS.		
19. SECURITY CLASSIF. (OF THIS REPORT) Unclassified	20. SECURITY CLASSIF. (OF THIS PAGE) Unclassified	21. NO. OF PAGES 82 + covers	22. PRICE

SI (METRIC) CONVERSION FACTORS

Approximate Conversions to SI Units				
Symbol	When you know	Multiply by	To Find	Symbol
		LENGTH		
in	inches	25.40	millimeters	mm
ft	feet	0.3048	meters	m
yd	yards	0.9144	meters	m
mi	miles	1.609	kilometers	km
		AREA		
in^2	square inches	645.2	square millimeters	mm
ft^2	square feet	0.0929	square meters	m^2
yd^2	square yards	0.8361	square meters	m^2
ac	acres	0.4047	hectares	ha
mi^2	square miles	2.590	square kilometers	km^2
		VOLUME		
fl oz	fluid ounces	29.57	milliliters	mL
gal	gallons	3.785	liters	L
ft^3	cubic feet	0.0283	cubic meters	m^3
yd^3	cubic yards	0.7645	cubic meters	m^3
		MASS		
oz	ounces	28.35	grams	g
lb	pounds	0.4536	kilograms	kg
T	short tons (2000 lb)	0.907	megagrams	Mg
		TEMPERATURE (exact)		
°F	degrees Fahrenheit	(°F-32)/1.8	degrees Celsius	°C
		FORCE and PRESSURE or STRESS		
lbf	poundforce	4.448	Newtons	N
lbf/in^2	poundforce per square inch	6.895	kilopascals	kPa

Approximate Conversions from SI Units				
Symbol	When you know	Multiply by	To Find	Symbol
		LENGTH		
mm	millimeters	0.0394	inches	in
m	meters	3.281	feet	ft
m	meters	1.094	yards	yd
km	kilometers	0.6214	miles	mi
		AREA		
mm^2	square millimeters	0.00155	square inches	in^2
m^2	square meters	10.764	square feet	ft^2
m^2	square meters	1.196	square yards	yd^2
ha	hectares	2.471	acres	ac
km^2	square kilometers	0.3861	square miles	mi^2
		VOLUME		
mL	milliliters	0.0338	fluid ounces	fl oz
L	liters	0.2642	gallons	gal
m^3	cubic meters	35.315	cubic feet	ft^3
m^3	cubic meters	1.308	cubic yards	yd^3
		MASS		
g	grams	0.0353	ounces	oz
kg	kilograms	2.205	pounds	lb
Mg	megagrams	1.1023	short tons (2000 lb)	T
		TEMPERATURE (exact)		
°C	degrees Celsius	9/5+32	degrees Fahrenheit	°F
		FORCE and PRESSURE or STRESS		
N	Newtons	0.2248	poundforce	lbf
kPa	kilopascals	0.1450	poundforce per square inch	lbf/in^2

ACKNOWLEDGEMENTS

- Funding Agency: OkTC OTCREOS9.1-36

- The authors appreciate Mr. Walt Peters from ODOT Bridge Division for his support and technical guidance offered to our work

- The field testing crew from the ODOT Bridge Division led by Mr. Wes Kellogg is appreciated

- Mr. Adrian Brügger, lab manager in the Department of Civil Engineering & Engineering Mechanics (CEEM) at Columbia University, is appreciated for his participation to and help for the field testing

- The following students who participated in the field testing are acknowledged: Randy D. Martin, former Master Student from the School of Civil Engineering & Environmental Science (CEES) at the University of Oklahoma (OU); Rami Akkari, Ph.D. Student from the School of Electrical & Computer Engineering (ECE) at OU; Dr. Lin Tang, former Ph.D. Student from ECE at OU; Winston Liu, Ph.D. Student from the Department of Computer Science (CS) at the Oklahoma State University (OSU); Keith Hurdelbrink and Amy Hufnagel, former undergraduate students from the School of Aerospace and Mechanical Engineering (AME) at OU and CEES at OU, respectively

STRUCTURAL IDENTIFICATION OF A REAL-WORLD SHEAR-CRITICAL PRESTRESSED CONCRETE HIGHWAY BRIDGE

Final Report

August 31, 2012

Peng F. Tang

Ph.D. Student

Jin-Song Pei

Ph.D., Associate Professor, Principal Investigator

Andrew W. Smyth

Ph.D., Professor

Luther W. White

Ph.D., Professor, Co-Principal Investigator

Sponsoring agency:

Oklahoma Transportation Center

2601 Liberty Parkway, Suite 110

Midwest City, Oklahoma 73110

Table of Contents

1. INTRODUCTION 1

1.1. Motivations and Technical Challenges 1

1.2. Overview of Accomplished Work 1

1.3. Overview of Key Findings 2

1.4. Structure of Report 3

2. BACKGROUND INFORMATION AND LITERATURE REVIEW 4

2.1. On Little River overflow bridge 4

2.2. Literature Review of Structural Health Monitoring of Similar Bridges 6

2.3. Terminologies for Data Acquisition System 7

2.4. Digital Signal Processing: A Snapshot 9

2.4.1. Definition of PSD 9
2.4.2. Periodogram 11
2.4.3. Estimation of PSD with MATLAB Toolbox 12

3. FIELD TESTING 15

3.1. Test Setup 15

3.2. Instrumentation 17

4. DATA PROCESSING 22

4.1. Overview of Data Processing 22

4.2. Preprocessing 22

4.3. Time-Domain Analysis of Etna Data 28

4.4. Frequency-Domain Analysis of Etna and SD Data 29

4.4.1. Overview 29
4.4.2. Comparison of Different Estimations for PSD 31
4.4.3. Extracting Representative Frequencies: Normalized PSD 33
4.4.4. Extracting Representative Frequencies: Coherence Function 38
4.4.5. Relative Motions - Elastic Deformations 40
4.4.6. Understanding Impact of Nonstationarity 42
4.4.7. Comparison of Etna and SD Data 44

5. RESULT ANALYSIS 48

5.1. Overview of Result Analysis 48

5.2. Validation of Modal Frequencies in Vertical Motion using Simplified Beam Model 49

5.3. Validation of Low-Frequency Motion in Transverse Motion using Simplified SDOF Model 51

5.4. Validation of Low-Frequency Motion in Longitudinal Motion using Simplified Analysis 52

5.5. Discussion of Consolidated PSD using Simplified LTI System Model 53

5.6. Understanding Experimental Observation: Quantifying Lateral and Longitudinal Motions at Low Frequencies 54

5.7. Understanding Experimental Observation: Lateral Motion Perceived by Human 56

6. OTHER WORK 57

6.1. Finite Element Modeling of Typical Span of Little River overflow bridge 57

6.2. Backbone Techniques 58

6.3. Inverse Problem 60

6.4. Markov Chain Monte Carlo Simulation 61

7. CONCLUSIONS 63

8. RECOMMENDATIONS FOR FUTURE WORK 64

9. References 65

List of Figures

Figure 1. The Little River overflow bridge (“Bridge D,” NBI No. 19269). 4
Figure 2. Elevation of the Little River overflow bridge (“Bridge D,” NBI No. 19269). 5
Figure 3. Typical expansion joint and simple support of the Little River overflow bridge (“Bridge D,” NBI No. 19269). 5
Figure 4. Piles and pile cap at a typical bent of the Little River overflow bridge (“Bridge D,” NBI No. 19269). 6
Figure 5. Illustrative example of how FT works inspired by an example in MATLAB. ... 10
Figure 6. IDs for columns and spans of the Little River overflow bridge. Highlighted are those involved in the field testing. 15
Figure 7. Plan view of a span of the Little River overflow bridge highlighting the lane closure required for testing. 15
Figure 8. Picture of the ODOT truck (left) and the Hydra platform trailer (right). 16
Figure 9. Dimensions of wheel loads for the truck and trailer. 16
Figure 10. Picture of the Hydra platform being positioned for a specific location. Note that the ODOT truck is completely off the span. 17
Figure 11. Layout of Etna and SD sensors. 19
Figure 12. (a)Four units of Etna on Span 4 during the test, and (b) to (d) show the base station, one end unit and the unit on the span - all of the SD sensors. 20
Figure 13. A comparison of Etna and SD data. It shows clearly that the resolution of Etna sensor is much higher than that of the SD sensor. 21
Figure 14. Flowchart illustrating the data processing efforts in this study. 22
Figure 15. Raw voltage time histories from all six SD sensors from 13:25 to 13:39 sampled at 200 Hz. 23
Figure 16. Relative acceleration time histories in y and z based on three plots in blue in Figure 15. 24
Figure 17. Zoomed-in views of Figure 16. 24
Figure 18. Acceleration time history for Test 134838: absolute value in transverse direction. The red boxes refer to the segments that are to be analyzed afterwards. 25
Figure 19. Acceleration time history for Test 134838: absolute value in longitudinal direction. 25

Figure 20. Acceleration time history for Test 134838: absolute value in vertical direction. 26
Figure 21. Zoomed-in views of Figure 18. 26
Figure 22. Zoomed-in views of Figure 19. 27
Figure 23. Zoomed-in views of Figure 20. 27
Figure 24. Comparison of PSD estimates for acceleration history of Channel 2 in x-direction. 32
Figure 25. Comparison of PSD estimates for acceleration history of Channel 2 in y-direction. 32
Figure 26. Comparison of PSD estimates for acceleration history of Channel 2 in z-direction. 33
Figure 27. PSD estimation of the data in the three directions and from all four channels of Test 134838 by using the Welch's method. 34
Figure 28. Normalized PSD estimation for four channels of Test 134838 in all three directions. 35
Figure 29. Consolidated NPSD estimation for each of the three directions in Test 134838. 37
Figure 30. Estimated coherence functions between all four channels within each direction. 39
Figure 31. Samples of the estimated coherence functions for all four channels in certain directions. 40
Figure 32. NPSD estimations for relative transverse motion. The vertical dash lines represent the locations of low frequency peaks for absolute motion. 41
Figure 33. NPSD estimations for relative longitudinal motion. The vertical dash lines represent the locations of low frequency peaks for absolute motion. 42
Figure 34. Sample results from the so-called piecewise analysis for Boxes 1, 7, 8 and 9 in x. 43
Figure 35. Comparison of NPSD of absolute motion at the south support. 44
Figure 36. Comparison of NPSD of absolute motion at the north support. 45
Figure 37. Comparison of NPSD of absolute motion at one-third span. 45
Figure 38. Comparison of NPSD of relative motion at one-third span. 46

Figure 39. A model of a simply-supported beam. 49
Figure 40. A picture taken from underneath Span 4 during the field testing, where we can observe the water table. 52
Figure 41. The filtered acceleration, estimated velocity and estimated displacement of 2.54 Hz in x and 1.37 Hz in y for Channel 4 of Test 134838. 55

List of Tables

Table 1. An overview of accomplished work during the period of this project. 2

Table 2. Summary of publications on vibration-based health monitoring of bridges........ 7

Table 3. A summary of different types of FT following [1]. † $j = \sqrt{-1}$. ‡ N is the length of the signal.. 9

Table 4. PSD estimation methods provided in MATLAB toolbox.................................. 14

Table 5. Comparison of the Burg (pburg), covariance (pcov), modified covariance (pmcov), and Yule-Walker methods (pyulear). 14

Table 6. Truck and trailer weights according to information from Wes Kellogg and Terex (manufacturer of the Hydra Platform), respectively. 17

Table 7. The format of the Etna data, where the number in the table shows the column number in each data set. 24

Table 8. Maximum Acceleration, i.e., $|x|$, from the recorded time histories. † Channel 1 data for this test is neglected... 29

Table 9. Peak frequencies with their normalized power levels for Test 134838. 36

Table 10. Estimated modal frequencies using a simple beam model............................ 50

Table 11. Amplitudes of the filtered acceleration, estimated velocity, estimated displacement of 2.54 Hz in x and 1.37 Hz in y for all but one Etna data sets. 55

Table 12. The range for properties of materials according to literature. 58

Table 13. Many faces of the bias/variance dilemma based on the triangle inequality. .. 61

Table 14. Pseudo-code of what was developed during the project period following the transitional Markov chain Monte Carlo (TMCMC) [48, 49].. 62

Executive Summary

A typical span of the Little River overflow bridge located in McCurtain County, Oklahoma, a shear-critical prestressed concrete bridge identified by the Oklahoma Department of Transportation (ODOT) Bridge Division, is studied using a multidisciplinary approach. Field measurements are collected in terms of accelerations. They are processed in both time-domain and frequency-domain analyses. The results are validated and interpreted using the principles in structural engineering to reveal the insights about the bridge span; new findings are discovered and reported to the ODOT Bridge Division. These findings and our developed systematic approach will be widely disseminated in the ASCE structural health monitoring community given the inherent challenge in processing and understanding dynamic measurements of real-world structures.

This case study would serve as a convincing example to demonstrate the usefulness of applying vibration-based structural health monitoring approach – when it is used to capture the behavior of a real-world structure in a global sense. With equal importance, this case study indicates the importance of integrating closely digital signal processing techniques with the knowledge in bridge design and modeling in order to make sense of the dynamic measurements of large-scale civil infrastructures.

These data processing and result analysis efforts are the focus of this report, while snapshots of our other work, including finite element modeling of the bridge span, nonlinear system identification and model updating, are provided. The limitations of vibration-based structural health monitoring approach are well known in the ASCE structural health monitoring, therefore continuing to develop novel solutions is needed.

Keywords: structural health monitoring, prestressed concrete bridge, ambient vibrations, vibration-based methods, frequency-domain analysis, nonstationarity of data.

1. INTRODUCTION

1.1. Motivations and Technical Challenges

We put forth a research project on structural health monitoring of prestressed concrete highway bridges with focuses on data processing, result interpretation and finite element model updating. We propose to thoroughly study a typical span of the Little River overflow bridge located in McCurtain County, Oklahoma, a shear-critical prestressed concrete bridge clearly identified by the Oklahoma Department of Transportation (ODOT) Bridge Division. Specifically, the interior girders were designed for shear following the 11th edition of AASHTO Standard Specifications in 1973 [2] but were found insufficient according to currently used AASHTO LRFD [3].

Shear failures are catastrophic in nature. According to the ODOT Bridge Division, there are prestressed concrete bridge girders with similar concerns in Oklahoma. Replacing them all or even retrofitting them all for shear would at least cost several millions of dollars. The required biennial inspection also incurs nontrivial cost. The actual shear capacity of these girders is therefore of a great deal of interest to the practice and decision-making for the ODOT Bridge Division.

Structural heath monitoring (SHM) has been making strides in the past decade or so as the health of the infrastructures continues to deteriorate [4]. To address the concern of the ODOT Bridge Division to the actual shear capacity of the specified girders in use, a structural identification approach should be adopted.

1.2. Overview of Accomplished Work

Our accomplished work is summarized in Table 1 following the proposed tasks in the proposal. All tasks planned in the proposal are carried out with serious effort; all of them have written documentations.

Table 1. An overview of accomplished work during the period of this project.

Task in Proposal	Work in Report	Work Documented Elsewhere and Remark
1	see Section 3 for details	an internal report led by Randall D. Martin in 2009
2a	see Section 6.1 for a snapshot	a separate write-up by Luther W. White
2b	see Section 8 for summary and recommendation	a separate write-up by Mr. Peng F. Tang in 2010
3	see Section 6.2 for Summary	(i) an internal report by Jin-Song Pei and Peter H. Fobel in 2011 (ii) an internal report by Ronald Adomako with contributions from Peng F. Tang, Joseph P. Wright and Jin-Song Pei in 2011 (iii) a journal paper draft by Peng F. Tang, Jin-Song Pei, Joseph P. Wright and Peter H. Fobel under preparation
4	see Section 6.3 for a snapshot	a separate write-up by Luther W. White
5	see Sections 4 and 5 for details	(i) a journal paper draft by Peng F. Tang, Jin-Song Pei, Luther W. White, and Andrew W. Smyth under preparation (ii) expected and unexpected findings thus the focus of this report
6	see Section 6.4 for a snapshot	an unfinished journal paper draft by James L. Beck, Jin-Song Pei and Konstantin M. Zuev in 2010

1.3. Overview of Key Findings

The fundamental frequency of a typical span of the Little River overflow bridge is determined and validated using six sets of acceleration measurements, each of a long recording duration, while other higher modal frequencies are estimated. As expected, the fundamental frequency corresponds to the vertical motion; its values extracted from the processed data measurement are consistent with those estimated using the first principle.

Using the measured accelerations, two low frequencies are identified in terms of the absolute motions along the transverse and longitudinal directions, in which the transverse motion was felt by a few members of the field testing team. However, these two low frequencies basically both disappear in the relative motions with respect to the ends of the span. It is thus suspected that these frequencies correspond to some rigid body motions of the entire beam-slab system of the bridge deck. A series of efforts is carried out to make sense of these suspected rigid body motions possibly concerning how exactly the bridge span behaves under the specified testing condition, i.e., one lane was open for traffic while the other was closed for testing personnel.

1.4. Structure of Report

According to Table 2, the data processing and result analysis are the centerpiece of this report. They are in Sections 4 and 5, respectively. While Section 2 gives a review of relevant techniques used in data processing among others, Section 3 outlines the field testing to highlight how the data was collected. Section 8 discusses future work, and Section 7 concludes the report.

2. BACKGROUND INFORMATION AND LITERATURE REVIEW

2.1. On Little River overflow bridge

The Little river overflow bridge is located in McCurtain County between the cities of Broken Bow and Idabel on State Highway 70 (See Figure 1). Figure 2 indicates the Type II girders with a large beam spacing of 11'9", which causes the concern of the ODOT engineers given that it is a shear-critical prestressed concrete bridge clearly identified by the ODOT Bridge Division. Figures 3 and 4 will be utilized in our result analysis.

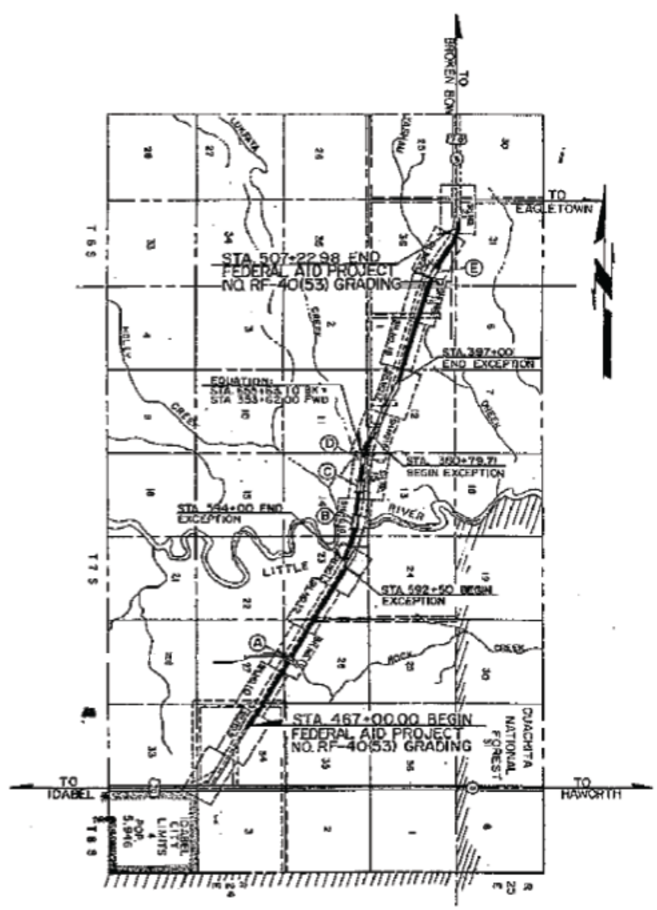

Figure 1. The Little River overflow bridge (“Bridge D,” NBI No. 19269).

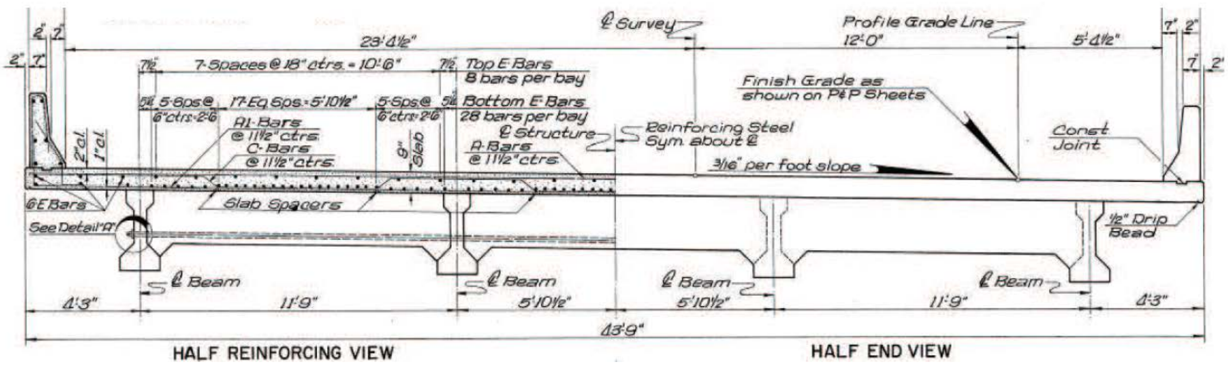

Figure 2. Elevation of the Little River overflow bridge ("Bridge D," NBI No. 19269).

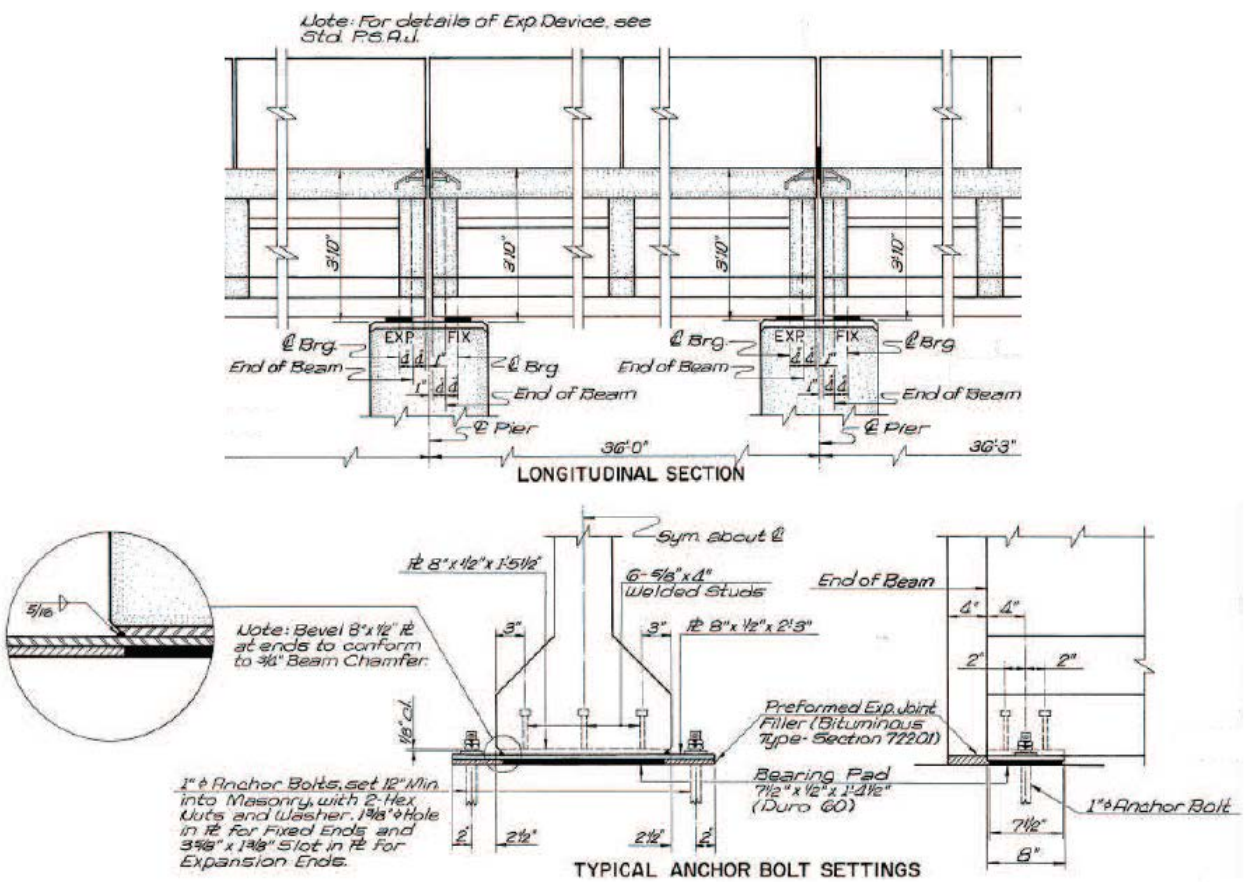

Figure 3. Typical expansion joint and simple support of the Little River overflow bridge ("Bridge D," NBI No. 19269).

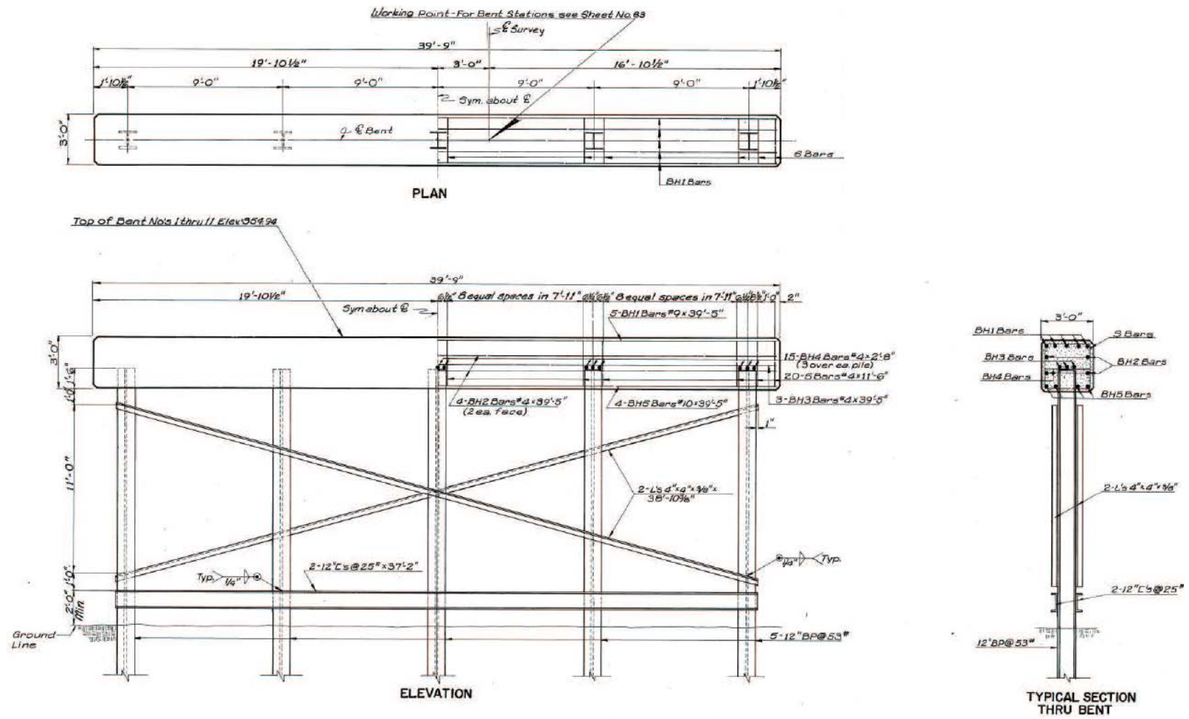

Figure 4. Piles and pile cap at a typical bent of the Little River overflow bridge ("Bridge D," NBI No. 19269).

2.2. Literature Review of Structural Health Monitoring of Similar Bridges

We searched the current literature on vibration-based structural health monitoring done on similar bridge structures and summarized it in Table 2.

Table 2. Summary of publications on vibration-based health monitoring of bridges.
† S-span, L-total length, W-width, T-thickness, H-height

Ref.	Nature of Bridge	Structural Type	Dimensions†	Freqs (Hz)	Sketch of Adopted Approach
[5]	unspecified	fixed-fixed	S=65.6', W=49.2', 7 webs (T=12'', H=5.6')	14.62 14.83 16.67	kinetic analysis using vibration modal analysis theory
[6]	unspecified	simply supported	3 spans, S=60', W=37.5', eight I-Beam tied with three diaphragms (T=6'') and two end diaphragms (T=15'')	4.04 6.26 11.97	finite element method using ANSYS
[7]	unspecified	unspecified	S=163', W=43.5', deck supported by two WF-36 steel plate girders and three WF-21 steel stringers	2.50 3.00 3.50	ambient test data analyzed by cross-correlation function method (Natural Excitation Technique, NExT)
[8]	highway bridge	unspecified	five spans, L=1089', three piers	1.61 2.06 2.64	standard Fourier transform
[9]	highway bridge	unspecified	three spans, L=196.6', W=41', two piers (53' apart from the central), deck: T=3'	3.24 5.32 8.40	finite element method and experiments using Frequency Response Function (FRF)
[10]	highway bridge	unspecified	6 spans, L=341', W=45', deck: T=3', three piers at each inner support	7.00 8.40 9.50	FRF

2.3. Terminologies for Data Acquisition System

Some of the main terminologies for the data acquisition system are given below:

Resolution: The smallest quantity that can be measured [11].

For example, an 18-bit resolution means the level of voltage that can be captured by the instrument is $1/2^{18}$ V, which is approximately 4×10^{-6} V.

Dynamic Range: The ratio between the largest and smallest possible values of a changeable quantity.

For electronics, it is the ratio of a specified maximum level of a parameter - denoted by “max” - such as power, current, voltage or frequency, to the minimum detectable value of that parameter - denoted by “min” (See Wikipedia: http://en.wikipedia.org/wiki/DynamicRange).

The formula for dynamic range is as follows:

$$\mathrm{DR} = 20\log_{10}\left(\frac{\max}{\min}\right) \tag{1}$$

Given that the maximum level of the voltage is 1 V and because the minimum level of voltage that can be captured by the instrument is $1/2^{18}$ V, the dynamic range would be as follows:

$$20 \times \log_{10}\left(\frac{\max}{\min}\right) = 20 \times \log_{10}(2^{18}) = 108\mathrm{dB}$$

which fits well with the description of the system on http://www.relemr-merc.org/Demo_Documentation.

Frequency Response: The relationship between the input and output.

The formula for frequency response $H(j\omega)$ of a system is as follows:

$$H(j\omega) = \frac{Y(j\omega)}{X(j\omega)} \tag{2}$$

where $Y(j\omega)$ and $X(j\omega)$ refer to the output and input in frequency-domain, respectively. In this study, the upper bound of the frequency response of the acquisition is 80 Hz. From Eq. (2), it can be seen that the output in this case can only be trusted in the frequency band below 80 Hz. This means we should only pay attention to the frequency components below 80 Hz.

Brickwall Filter: An idealized electronic filter, one that has full transmission in the passband, and complete attenuation in the stop band, with abrupt transitions, such as a sinc filter.

This is not physically realizable as it is an infinite impulse response (IIR) filter, but approximate implementations are sometimes used and they are frequently called Brickwall filters (See Wikipedia: http://en.wikipedia.org/wiki/Sinc_filter#Brick-wall_filters).

2.4. Digital Signal Processing: A Snapshot

2.4.1. Definition of PSD

To explain the meaning of *power spectral density (PSD)*, it is useful to introduce a commonly used technique, *Fourier transform (FT)*, which transforms a signal from time-domain to frequency-domain by describing how the signal is composed of different frequency components. Depending on the type of the signal, FT is defined differently. The relationship between a time signal x and its frequency counterpart X is summarized in Table 3 following [1]. Figure 5 is an example to illustrate how FT works: A discrete and finite signal in time-domain (left panel) is a two-component sine wave, $x = 0.7\sin(2\pi \times 10t) + \sin(2\pi \times 40t)$, corrupted with white noise. The signal's frequency response magnitude (right panel), which is done through DFT, has two outstanding peaks exactly at the two known frequencies, 10 Hz and 40 Hz.

Table 3. A summary of different types of FT following [1].
† $j = \sqrt{-1}$. ‡ N is the length of the signal.

Type of FT	Mathematical Expression	Type of Signal for Application
continuous FT (CFT)	$X(j\omega) = \int_{-\infty}^{\infty} x(t)e^{-j\omega t}dt$ †	continuous & infinite duration
discrete-time FT (DTFT)	$X(e^{j\omega}) = \sum_{n=-\infty}^{\infty} x[n]e^{-j\omega n}$	discrete & infinite duration
discrete FT (DFT)	$X\left[\frac{2\pi k}{N}\right] = \sum_{n=0}^{N-1} x[n]e^{-\frac{j2\pi kn}{N}}$ ‡	discrete & finite duration

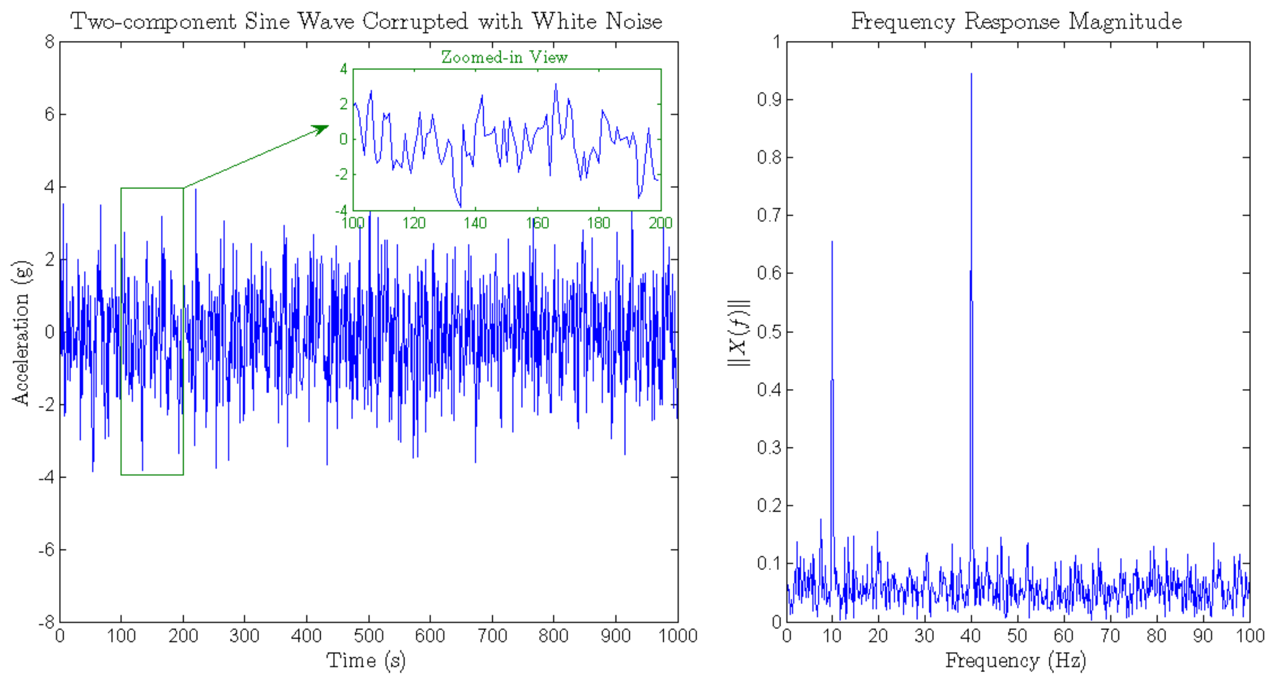

Figure 5. Illustrative example of how FT works inspired by an example in MATLAB.

From here, it would be easy for us to explain PSD, a useful quantity in frequency-domain analysis. The definition of PSD is as follows:

$$P_z(\omega) = \sum_{m=-\infty}^{\infty} R_z\,(m)e^{-j\omega m}$$

$$(3)$$

where

$$R_z(m) = \; E(z[n+m]z^*[n])$$

$$(4)$$

and $R_z(m)$ is the *auto-correlation* of $z[n]$, where E represents expectation and $*$ stands for *complex conjugate* [12]. Auto-correlation is a mathematical concept for finding repeating patterns, such as the presence of a periodic signal which is corrupted with noise. By comparing Eq. (3) with Table 2.4.1, it can be seen that $P_z(\omega)$ is in fact the DTFT of $R_z(m)$.

Cross-correlation is a quantity similar to auto-correlation, and is defined as follows:

$$R_{xy}(m) = E(x[n+m]y^*[n])$$
(5)

Its DTFT is called *cross-spectral density (CSD)*, and is computed as follows:

$$P_{xy}(\omega) = \sum_{m=-\infty}^{\infty} R_{xy}(m)e^{-j\omega m}$$
(6)

The coherence function of two signals, x and y, is the ratio of the magnitude square of their CSD over the product of their own PSDs expressed as follows:

$$\gamma_{xy}(\omega) = \frac{\left|P_{xy}(\omega)\right|^2}{P_x(\omega)P_y(\omega)}$$
(7)

For a physical system with frequency f in Hz, the *angular frequency* in Eq. (3) is as follows:

$$\omega = \frac{2\pi f}{f_s}$$
(8)

where f_s is the sampling frequency in Hz.

2.4.2. Periodogram

According to Eq. 3, the definition of PSD calls for the use of infinite-length signals. This is not possible for real-world applications; therefore, the PSD is commonly estimated through periodogram. *Periodogram* is the square of the magnitude of DFT and expressed as follows:

$$S_x\left(e^{j\omega}\right) = \frac{1}{N}\left|\sum_{n=0}^{N-1} x[n]e^{-j\frac{2\pi kn}{N}}\right|^2$$
(9)

where

$$\omega = \frac{2\pi k}{N}, \qquad k = 0, 1, \dots, N-1$$

in other words, ω is discretely and uniformly distributed [12].

Since periodogram is nothing but basic Fourier transform, it suffers from the problem of poor variance and bias behavior. When a windowing function is first applied to the data, a periodogram is called a modified periodogram, and is defined as follows:

$$S_x(e^{j\omega}) = \frac{\frac{1}{N}\left|\sum_{n=0}^{N-1} w[n]x[n]e^{-j\omega n}\right|^2}{\frac{1}{N}\sum_{n=0}^{N-1}|w[n]|^2} \tag{10}$$

where $w[n]$ is the so-called window function, the use of which helps ease the problem of frequency leaking involved in DFT and reduce the variance in the estimation of PSD.

Equation (10) follows the idea of a famous algorithm called the Welch's method, put forth in [13], which we depend heavily on for our data analysis. In the Welch's method, we used one commonly used window function, the Hamming window [14], which is defined as follows:

$$w[n] = 0.54 - 0.46\cos\left(\frac{2\pi n}{N-1}\right),\ n = 0,1,\dots,N \tag{11}$$

2.4.3. Estimation of PSD with MATLAB Toolbox

MATLAB [15] Signal Processing Toolbox provides three categories for PSD estimation methods as follows:

Nonparametric methods: Estimating PSD directly from the signal itself. The simplest such method is the Periodogram estimation. Other nonparametric techniques include the Welch's method and the multitaper method (MTM), both of which reduce the variance of the estimation.

Parametric methods: Estimating PSD from a signal assumed to be an output of a linear system driven by a white noise, which is also known as Autoregressive (AR) methods. They include the Yule-Walker autoregressive method, the Burg method, covariance method, and modified covariance method. An important parameter that needs to be specified for these methods is called the order of a system, which represents the input of how many time steps back could affect the current output.

Subspace methods: Generating frequency component estimates for a signal based on an eigenanalysis or eigendecomposition of the autocorrelation matrix. They are also known as high-resolution methods or super-resolution methods. They include the multiple signal classification (MUSIC) method or the eigenvector (EV) method. These methods will not be discussed hereafter.

Table 4 lists the methods and their MATLAB commands.

Table 4. PSD estimation methods provided in MATLAB toolbox.

Method	MATLAB Built-in Function
Periodogram	spectrum.periodogram, periodogram
Welch	spectrum.welch, pwelch, cpsd, tfestimate, mscohere
Multitaper	spectrum.mtm, pmtm
Yule-Walker AR	spectrum.yulear, pyulear
Burg	spectrum.burg, pburg
Covariance	spectrum.cov, pcov
Modified Covariance	spectrum.mcov, pmcov
MUSIC	spectrum, music, pmusic
Eigenvector	spectrum.eigenvector, peig

Table 5, adapted from [16], summarizes the features of the above-mentioned four AR methods.

Table 5. Comparison of the Burg (pburg), covariance (pcov), modified covariance (pmcov), and Yule-Walker methods (pyulear).

Fcns.	Characteristics	Advantages	Disadvantages	Singularity Conditions
pburg	No windowing for data Forward and backward prediction errors minimized in the least squares sense with the AR coefficients constrained to satisfy the L-D recursion	High resolution for short data records Always produces a stable model	Peak locations highly dependent on initial phase May having spectral line-splitting for sinusoids in noise or with very large order Freq. bias for estimates of sinusoids in noise	
pcov	No windowing for data Forward prediction error minimized in the least squares sense	Better resolution than Y-W for short data records Able to extract freq. from data consisting of p or more pure sinusoids	Unstable models possible Freq. bias for estimates of sinusoids in noise	Order less than or equal to half the input frame size & 2/3 the input frame size
pmcov	No windowing for data Forward and backward prediction errors minimized in the least squares sense	High resolution for short data records Able to extract freqs. from data consisting of p or more pure sinusoids	Unstable models possible Peak locations slightly dependent on initial phase Minor freq. bias for estimates of sinusoids in noise	Order less than or equal to half the input frame size & 2/3 the input frame size
pyulear	Windowing for data Forward prediction error minimized in the least squares sense (also called “autocorrelation method”)	Performing as well as other methods for large data records Always producing a stable model; not having spectral line-splitting	Relatively poor performance for short data records	Nonsingularity guaranteed due to positive definite autocorrelation matrix

3. FIELD TESTING

3.1. Test Setup

The goal of the instrumentation is to collect as much information as possible to enable data processing and result analysis by focusing on Span 4 as shown in Figure 6. One out of the two lanes was closed to facilitate testing as shown in Figure 7. During the field trip, we deployed wireless sensors as well as strain gauges as secondary instrumentation; however, we were not successful in obtaining meaningful results. Therefore we focus on our primary instrumentation, tethered accelerometers, herein.

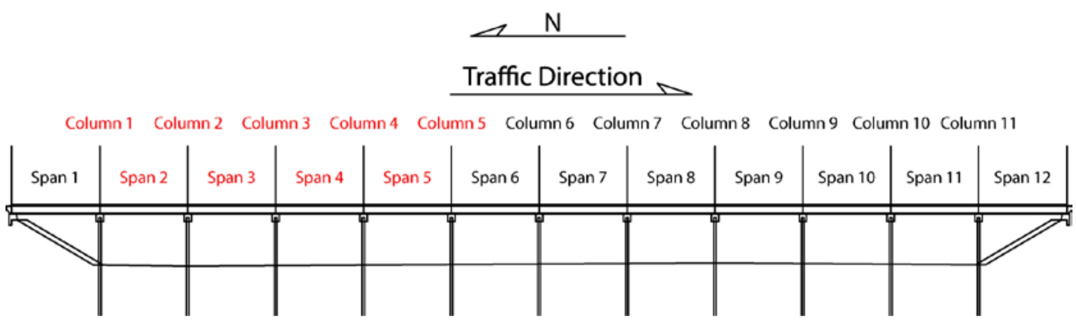

Figure 6. IDs for columns and spans of the Little River overflow bridge. Highlighted are those involved in the field testing.

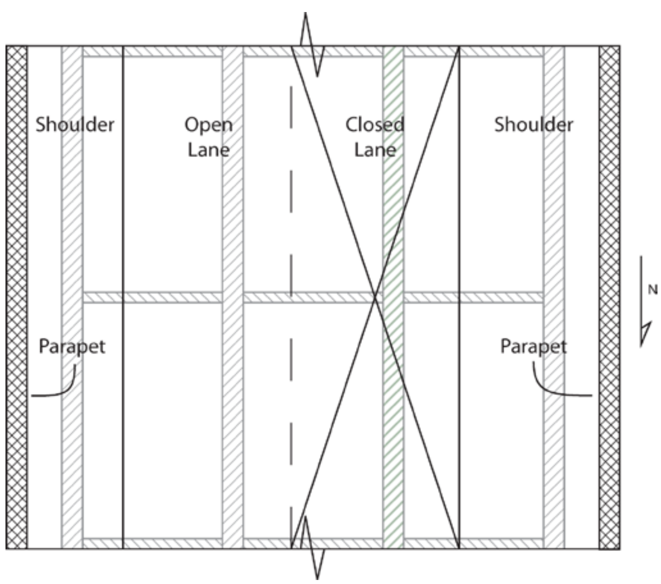

Figure 7. Plan view of a span of the Little River overflow bridge highlighting the lane closure required for testing.

Under the testing condition, the bridge was subject to both vehicle and wind-induced vibrations. Given the elevation of the bridge, we believe that it is a case when the vibration was dominated by vehicle-induced excitation. Pictures of the ODOT truck and Hydra Platform trailer are shown in Figure 8 and the Hydra Platform trailer positioned for a strain reading in Figure 10.

Figure 8. Picture of the ODOT truck (left) and the Hydra platform trailer (right).

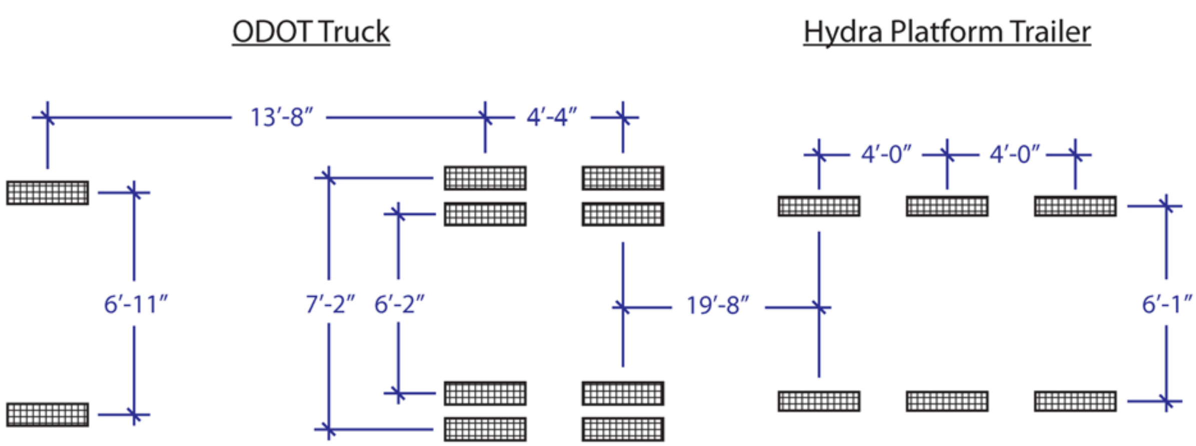

Figure 9. Dimensions of wheel loads for the truck and trailer.

Table 6. Truck and trailer weights according to information from Wes Kellogg and Terex (manufacturer of the Hydra Platform), respectively.

	Total Weight (pounds)	Wheel Loads (pounds)
Truck	18,480	4,000
Trailer	18,200	2,867

Figure 10. Picture of the Hydra platform being positioned for a specific location. Note that the ODOT truck is completely off the span.

3.2. Instrumentation

As shown in Figure 11, four units of tri-axial Etna High dynamic range strong motion accelerograph from Kinematics Inc. (http://www.relemr-merc.org/Demo_Documentation/Etna/Etna.htm abbreviated as “Etna” hereafter) were deployed on the bridge deck, while six numbers of uni-axial Silicon Designs Analog Accelerometer Module 2210-002 (abbreviated as “SD” hereafter) were installed on one side of an interior girder under the bridge deck. Every two SD sensors were packaged into one unit before the field testing; accelerations along two perpendicular directions can be measured using one unit.

As shown in Figure 11, four units of tri-axial Etna sensors, Channels 1 to 4, were deployed to Span 4 right on top of an interior girder. All of them were aligned as further shown in Figure 12(a). Channels 1 and 4 were assigned to the two ends of a span, while Channel 2 and 3, one-third and mid span, respectively. The intention for the layout of the three SD units, shown in Figure 11, is to match three out of the four Etna units for the sake of data analysis. However, due to the obstruction of a diaphragm beam at the girder end (see Figure 12(c)), the matching could not be done in a precise manner. Hence, the labels for the Etna units are 1 to 4 while those for the SD units are, 1’, 2’ and 4’.

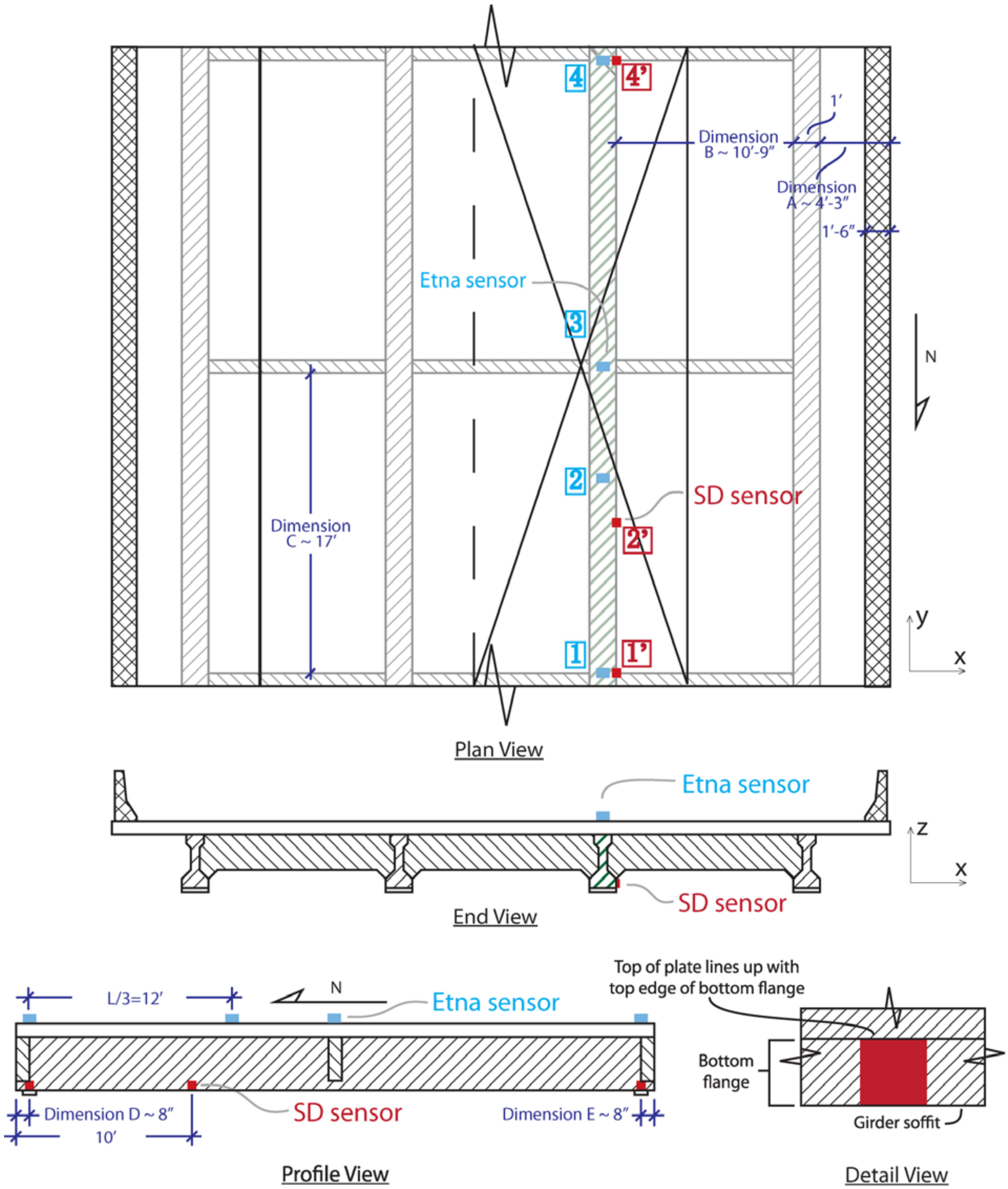

Figure 11. Layout of Etna and SD sensors.

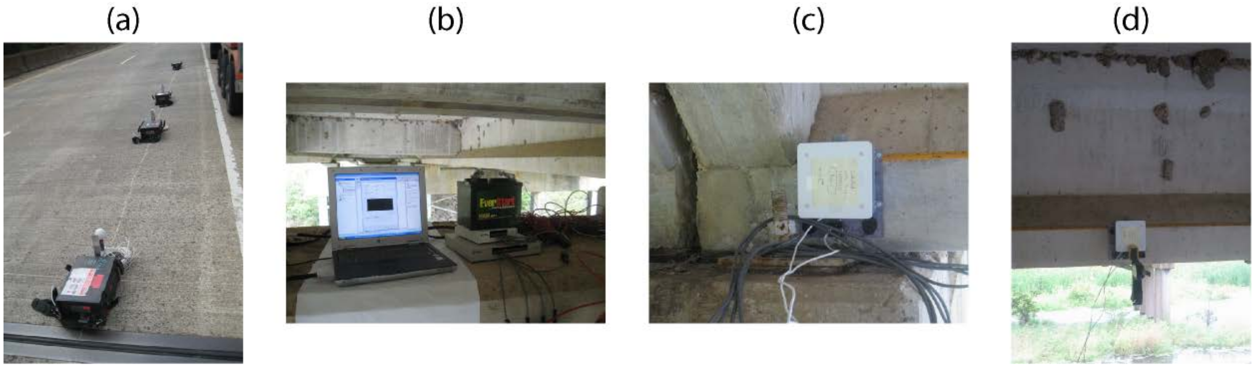

Figure 12. (a)Four units of Etna on Span 4 during the test, and (b) to (d) show the base station, one end unit and the unit on the span - all of the SD sensors.

More details concerning the instrumentation using the Etna sensors are given as follows:

Data sets Six, and they are denoted as 132558, 134838, 141656, 143454, 150504, 162550 following the starting time for data acquisition in term of “hhmmss”

Axis x transverse (east-west), y longitudinal (south-north), and z vertical (up and down)

Sampling rate $f_s = 200$ Hz

Sensitivity 1 g ≈ 2.5 V , and the precise sensitivity is given in every data set

Zero-g offset taken as the mean of the voltage output of some resting period(s) in each data set

Sensor location See Figure 11

During the field test, we coordinated so that two data sets coming from Etna and SD were collected during the same period of time, namely, 13:26 - 13:38 pm. Given their spatial relations described above, the collaborations of these two data sets would benefit the understanding of the entire structural system. Nonetheless, accurately synchronizing these two data sets would not be feasible given their different resolutions and clocks.

Figure 13 is designed to contrast the drastically different resolutions of these two sensors.

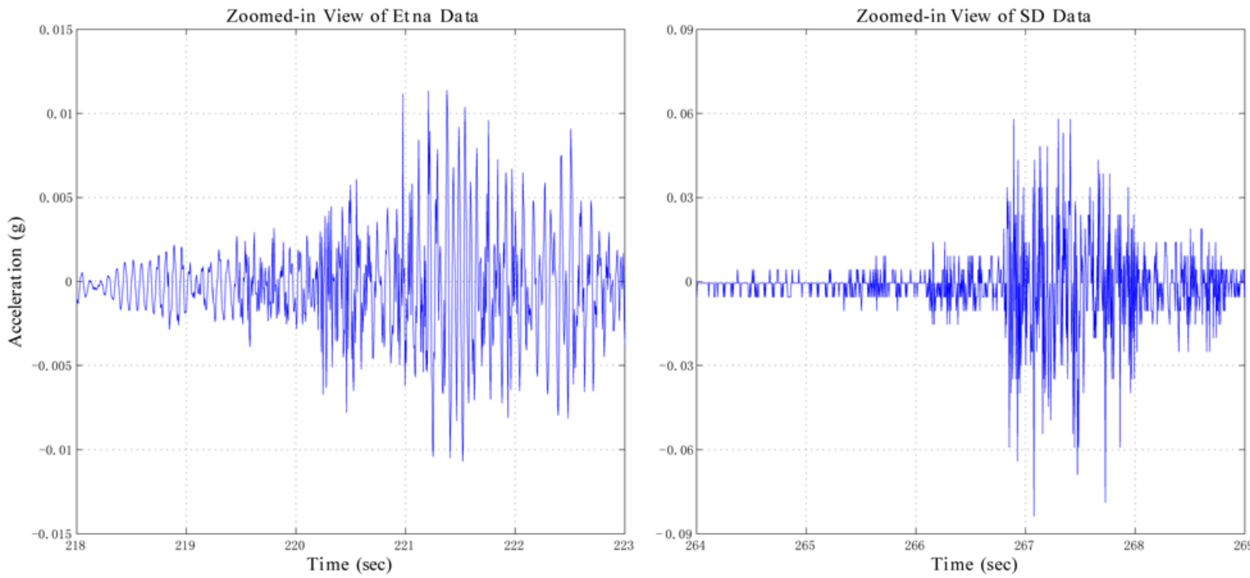

Figure 13. A comparison of Etna and SD data. It shows clearly that the resolution of Etna sensor is much higher than that of the SD sensor.

One important fact to highlight is that during the tests, Professor Andrew Smyth who has had extensive field testing experiences with cable suspension bridges in New York City, voiced out the transverse motions which he considered unusual. In the subsequent data processing and result analysis, we thus paid particular attention to the transverse motion, during which we encountered two low frequencies in the transverse and longitudinal directions.

4. DATA PROCESSING

4.1. Overview of Data Processing

The goal of data processing is to seek both the modal frequencies and aforementioned suspicious transverse motions. We followed the routine of preprocessing, and time-domain and frequency-domain analysis. However, the challenge of clearly identifying both the modal frequencies and the other suspicious issue called for quite some extensive efforts. A flowchart of data processing is shown in Figure 14. The structure of the analysis and the interrelations of the components are illustrated. All of the steps will be described in detail one after another.

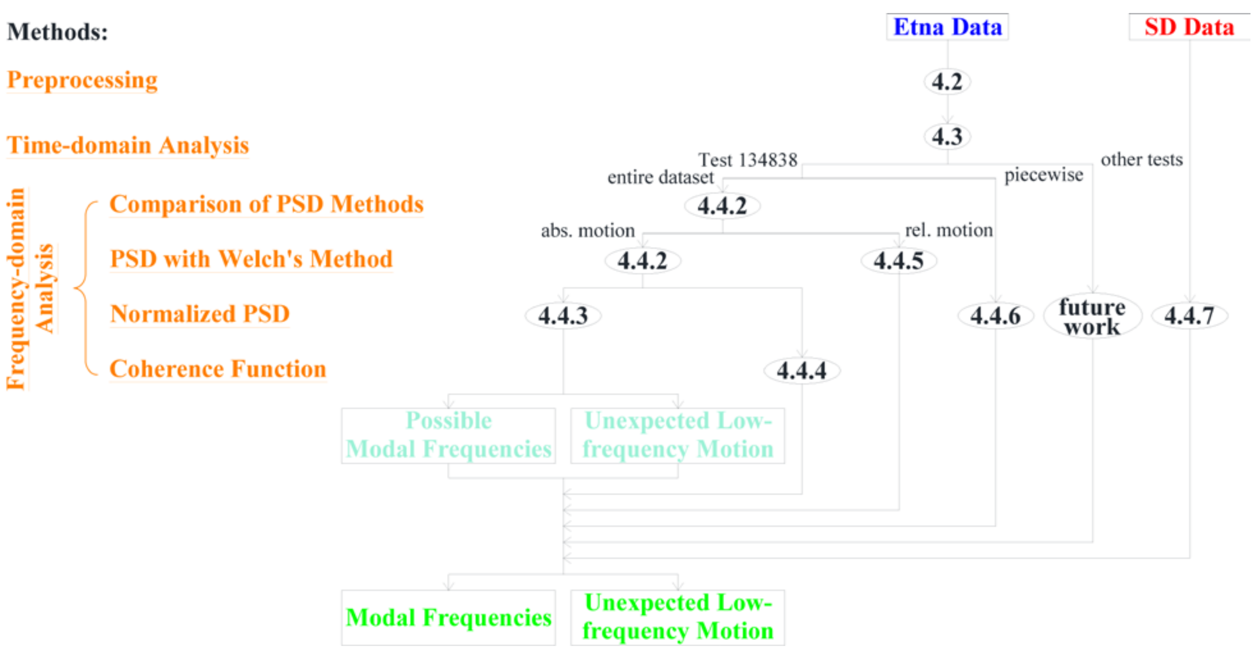

Figure 14. Flowchart illustrating the data processing efforts in this study.

4.2. Preprocessing

Following common practice, all voltage readings in this study were converted to the accelerations using the sensor's sensitivity and zero-g output as follows:

$$\text{acceleartion (g)} = (\text{voltage reading} - \text{zero/g voltage}) \times \text{sensitivity} \tag{12}$$

where sensitivity is the acceleration in g per voltage.

The relative acceleration at either one-third or half span with respect to the average of the two ends can be calculated as follows:

$$\text{relative acc} = \text{absolute acc} - \frac{\text{sum of absolute acc at two supports}}{2} \tag{13}$$

which applies to all three directions.

Some raw data collected from the SD sensors is shown in Figure 15. A sample relative acceleration time history for the SD sensors is presented in Figure 16, while a zoomed-in snapshot is given in Figure 17. For the SD raw data, there is a nontrivial DC drift, which was filtered out using a high-pass filter at the preprocessing stage.

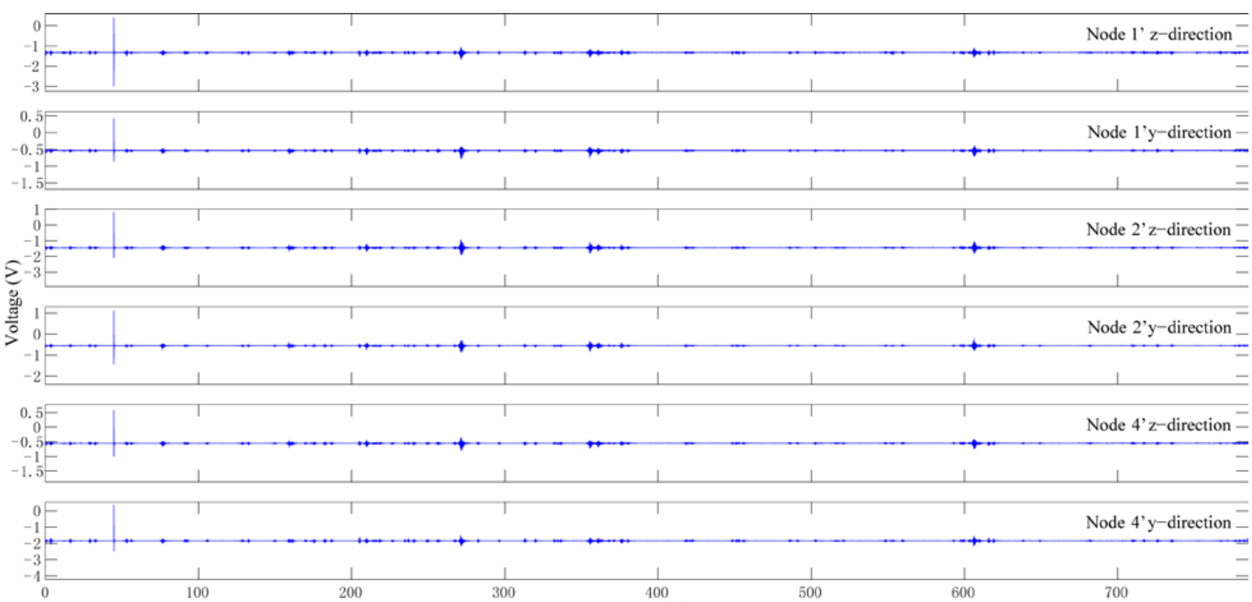

Figure 15. Raw voltage time histories from all six SD sensors from 13:25 to 13:39 sampled at 200 Hz.

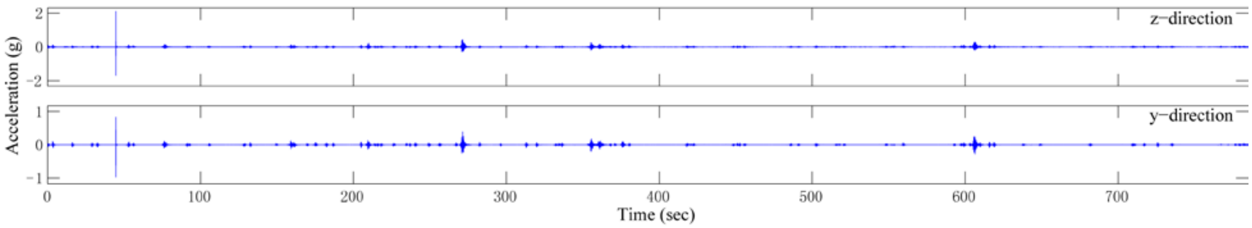

Figure 16. Relative acceleration time histories in y and z based on three plots in blue in Figure 15.

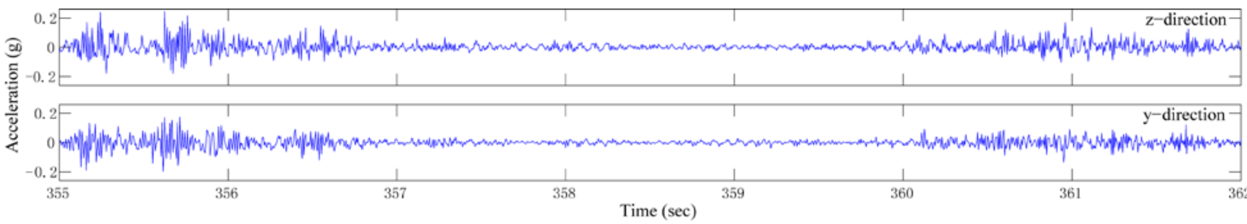

Figure 17. Zoomed-in views of Figure 16.

In terms of data format, details of the Etna are shown in Table 7:

Table 7. The format of the Etna data, where the number in the table shows the column number in each data set.

Direction	Channel 1	Channel 2	Channel 3	Channel 4
x	1	4	7	10
y	2	5	8	11
z	3	6	9	12

One out of six sets of recorded time histories using the Etna sensors is presented from Figure 18 to 20 after applying Eq. (12). The red boxes highlight some representative pieces to be analyzed later.

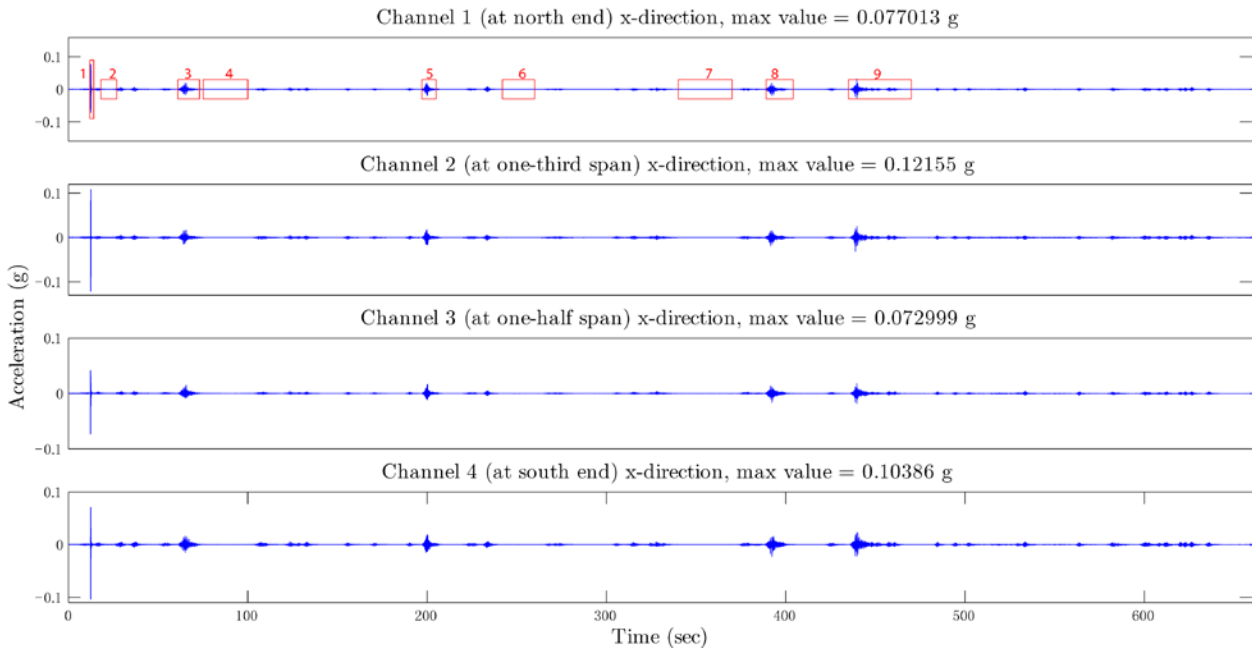

Figure 18. Acceleration time history for Test 134838: absolute value in transverse direction. The red boxes refer to the segments that are to be analyzed afterwards.

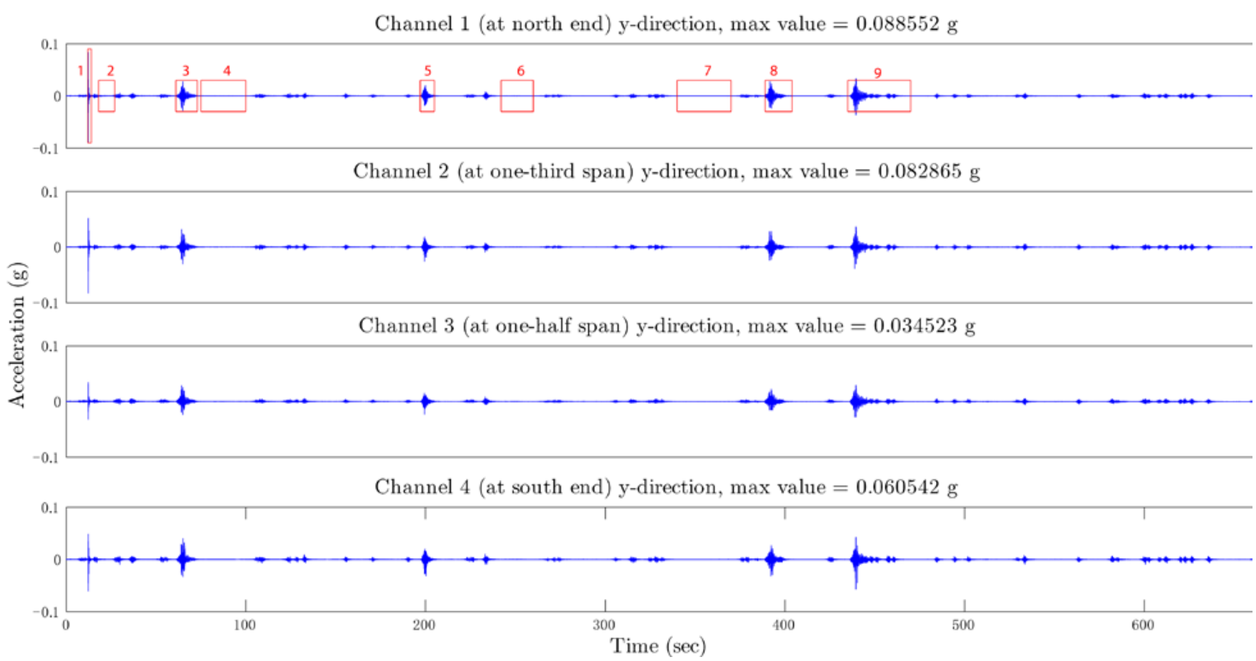

Figure 19. Acceleration time history for Test 134838: absolute value in longitudinal direction.

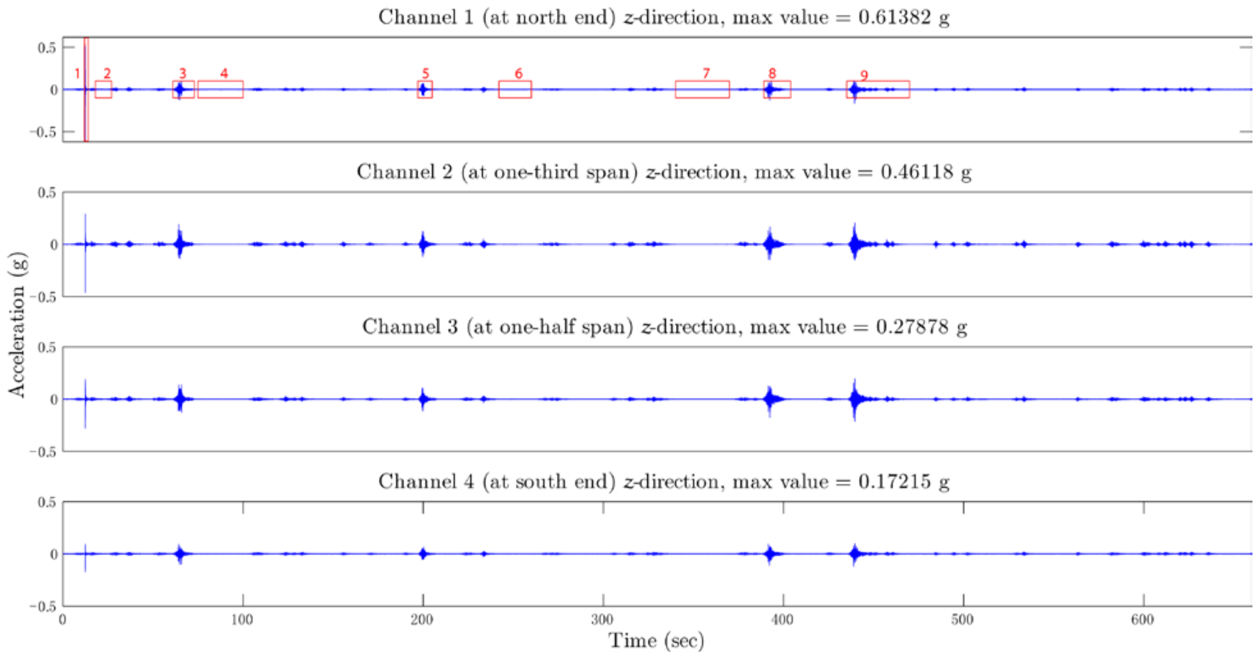

Figure 20. Acceleration time history for Test 134838: absolute value in vertical direction.

To have a better idea of the acceleration history, zoomed-in samples of Etna data of Test 134838 are given in Figures 21 to 23.

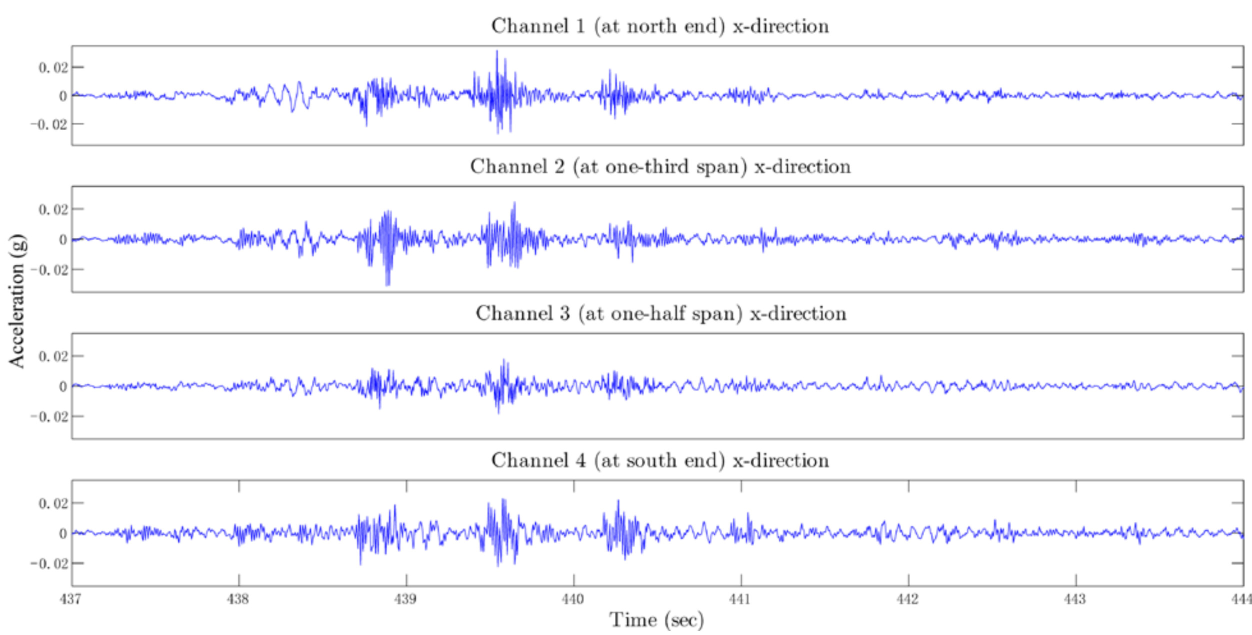

Figure 21. Zoomed-in views of Figure 18.

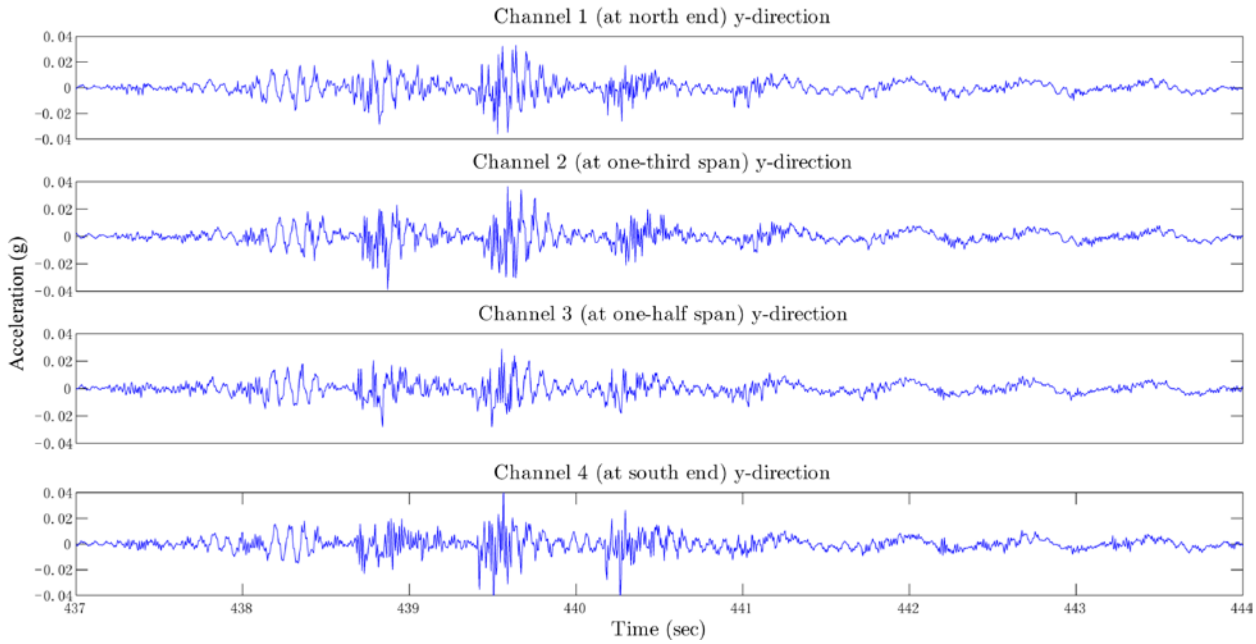

Figure 22. Zoomed-in views of Figure 19.

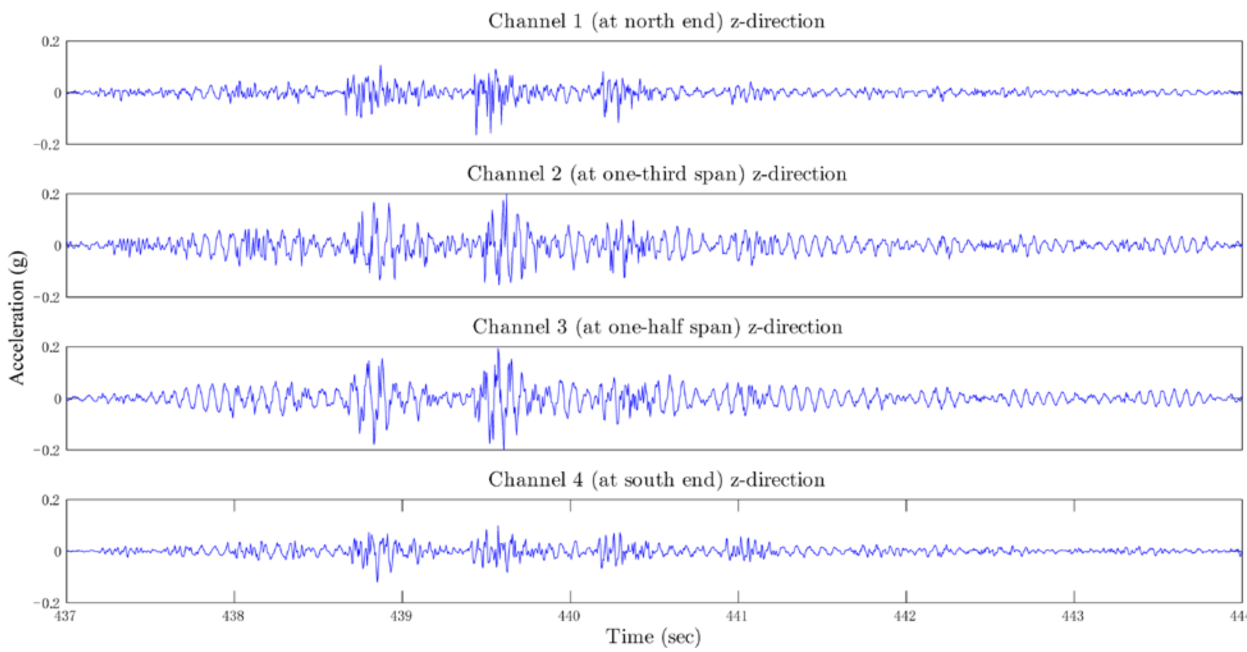

Figure 23. Zoomed-in views of Figure 20.

4.3. Time-Domain Analysis of Etna Data

For the test setup specified in Sections 3.1 and 3.2, the forced response of the typical bridge span superstructure is dominated with the vehicle-induced vibrations. The excitation (i.e., the input to the system) was not measured, and only the response (i.e., the output to the system) was measured.

After applying both Eqs. (12) and (13), the maximum values of the Etna data is presented in Table 4.3. It can be seen that:

- The measured responses are not stationary given the nature of vehicle-induced vibrations.
- The vibration along z dominates, which was anticipated.
- The range of the acceleration values along z seems normal [17].
- The vibrations along x and y need further confirmation including comparisons with relevant literature and the FEM modeling of this particular bridge span.

The damping for the first mode was estimated to be in the range of 8% to 10%.

Table 8. Maximum Acceleration, i.e., $|\ddot{x}|$, from the recorded time histories. † Channel 1 data for this test is neglected.

Channel	Absolute Measurement (g)			Relative Motion (g)		
	Transverse (x)	Longitudinal (y)	Vertical (z)	Transverse (x)	Longitudinal (y)	Vertical (z)
Test 132558 on Span 4						
1	0.026961	0.042323	0.086039	NA	NA	NA
2	0.039934	0.044170	0.162340	0.044568	0.059139	0.207920
3	0.043049	0.040562	0.160920	0.055699	0.034528	0.171890
4	0.027166	0.037816	0.131170	NA	NA	NA
Test 134838 on Span 4 (with Modal Hammer)						
1	0.077013	0.088552	0.613820	NA	NA	NA
2	0.121550	0.082860	0.461180	0.1466400	0.087845	0.556270
3	0.072999	0.034523	0.278780	0.0658890	0.054552	0.512150
4	0.103860	0.060542	0.172150	NA	NA	NA
Test 141656 on Span 4						
1	0.022166	0.036046	0.131960	NA	NA	NA
2	0.019503	0.037257	0.248330	0.026989	0.048132	0.254310
3	0.018403	0.028830	0.154020	0.027411	0.029149	0.171090
4	0.056155	0.050913	0.093273	NA	NA	NA
Test 143454 on Span 4						
1	0.023632	0.030440	0.089677	NA	NA	NA
2	0.027628	0.029883	0.110560	0.041166	0.045177	0.142160
3	0.026233	0.028282	0.133690	0.033916	0.030454	0.144200
4	0.024009	0.038925	0.102790	NA	NA	NA
Test 150504 on Multiple Spans						
2	0.029681	0.032311	0.125190	NA	NA	NA
3	0.021123	0.026078	0.134770	NA	NA	NA
4	0.032126	0.037316	0.112890	NA	NA	NA
Test 162550 on Span 4						
1	0.049434	0.031004	0.088397	NA	NA	NA
2	0.029578	0.032935	0.213320	0.044969	0.040844	0.193150
3	0.037526	0.028417	0.155440	0.036980	0.041147	0.157090
4	0.024934	0.041207	0.094679	NA	NA	NA

4.4. Frequency-Domain Analysis of Etna and SD Data

4.4.1. Overview

An overview of the frequency-domain analysis has been presented as part of the data processing previously in Figure 14. Simplified structural analysis was carried out before and during the data processing to predict what to anticipate and illuminate insights; however, simplified structural analysis will not be elaborated here for clarity in presentation.

First of all, the typical bridge span superstructure is a monolithic beam-slab structural system as shown in Figures 2 and 7. For the beams, there are girders and diaphragms. For the slab, the overall dimensions are 36’ (span) by 43’9” (width) while each panel measures 11’9” by 18’. If the fundamental mode shape is assumed to be in-plane bending, both the z (vertical) and x (transverse) directions are anticipated to participate in this mode. In other words, the fundamental modal frequency should be seen in all z, x, and y (longitudinal) directions. Along this line of thinking and considering the rigidity of the monolithic beam-slab system under study, we will be looking for peak frequencies that are in common for all three directions. This is why we utilize the so-called normalized PSD (to be elaborated) and coherence function to condense a wide range of results directly from applying the PSD.

As mentioned previously, the forced response created during the field testing was dominated with the driving vehicles from one driving lane. We thus anticipate to see the motions in z to dominate, which has been confirmed in the time-domain analysis. Simplified analysis considering only z reveals a fundamental modal frequency in the order of 10, a reference threshold for the fundamental modal frequency of the entire system under study.

Here we are set to apply FT-based methods that are only suitable for periodic and stationary signals to non-stationary measurements. This would be the first major source of errors. To understand the impact to the results of the frequency-domain analysis from using the nonstationary measurements, we will not only use an entire time history but also carefully select representative pieces of the same time history for PSD estimation. We call the latter “piecewise analysis.”

Following Section 2.4, PSD can only be estimated given the finite length of any real-world signal. This is the inherent limitation that we have to deal with. Previous studies (e.g., [18]) compare different PSD methods; here we will first verify the comparison by testing a series of PSD methods on one typical Etna data set before using only the

Welch's method throughout the rest of this study. In addition, we bear in mind the influence of the type and length of the window function to the processed result when we choose to stick with one type of window function that has a fixed window length in almost all cases.

Another source of errors comes from the fact that we only have the response (i.e., output) spectrum of the system. We do not have the frequency response function (FRF) given that we did not and could not measure the excitation (input) to the system. If the input was white noise, then the output spectrum would be the FRF spectrum. The output spectrum has the modal frequencies that we are seeking; however, it also has other characteristics of the forcing function - the fact of which we need to bear in mind. The aforementioned piecewise analysis helps understand the impact from different forcing functions.

4.4.2. Comparison of Different Estimations for PSD

To better understand the various methods for PSD estimation, a total of seven methods discussed previously in Section 2.4.3 were applied to the entire time histories shown in Figure 18 to 20. The processed results are presented in Figure 24 to Figure 26. In these exercises, the order for the parametric methods were all assumed to be 100 based on trial and error.

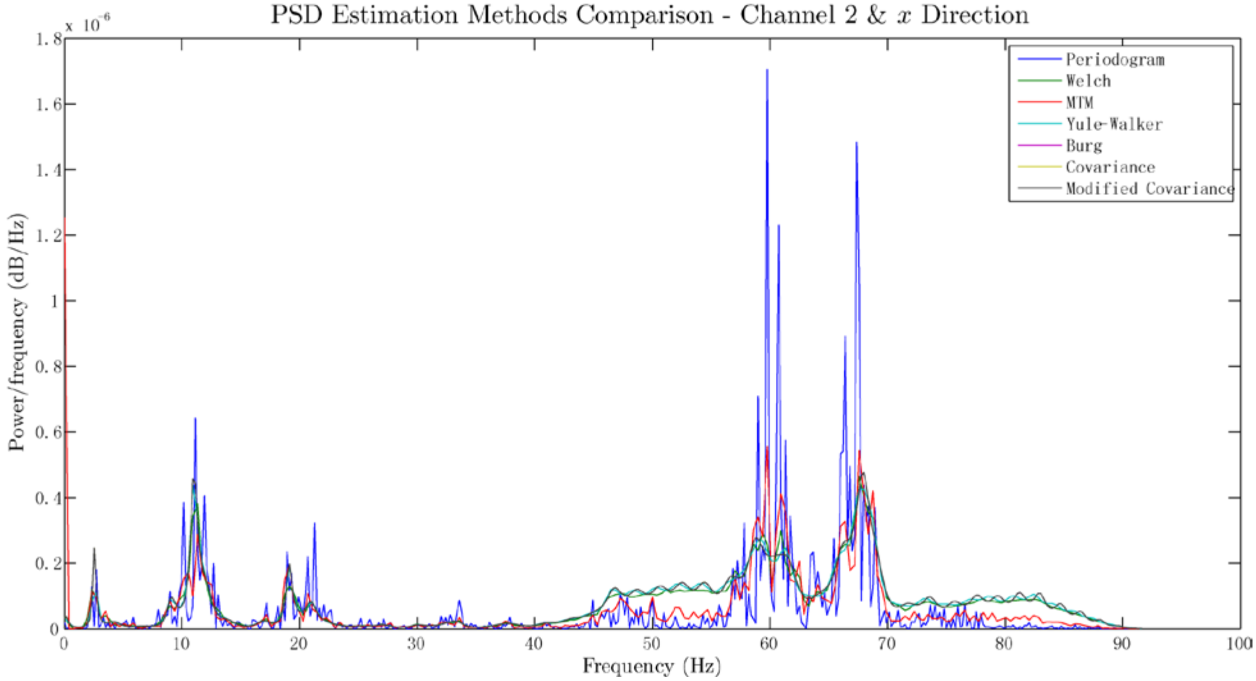

Figure 24. Comparison of PSD estimates for acceleration history of Channel 2 in x-direction.

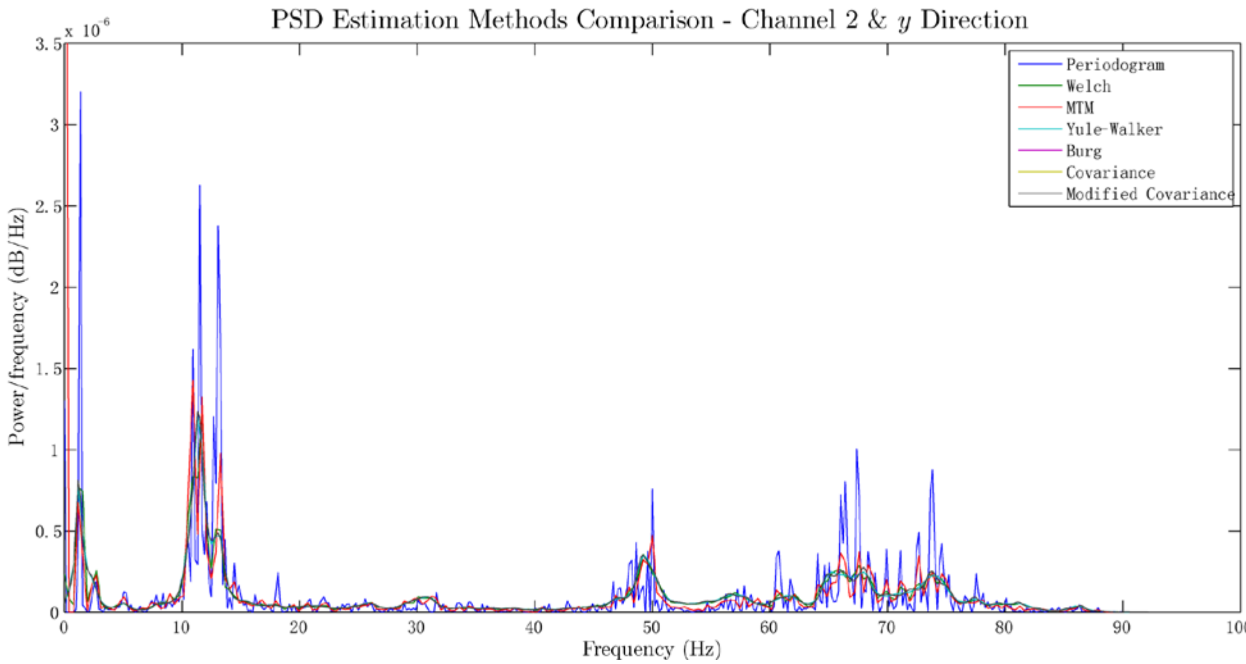

Figure 25. Comparison of PSD estimates for acceleration history of Channel 2 in y-direction.

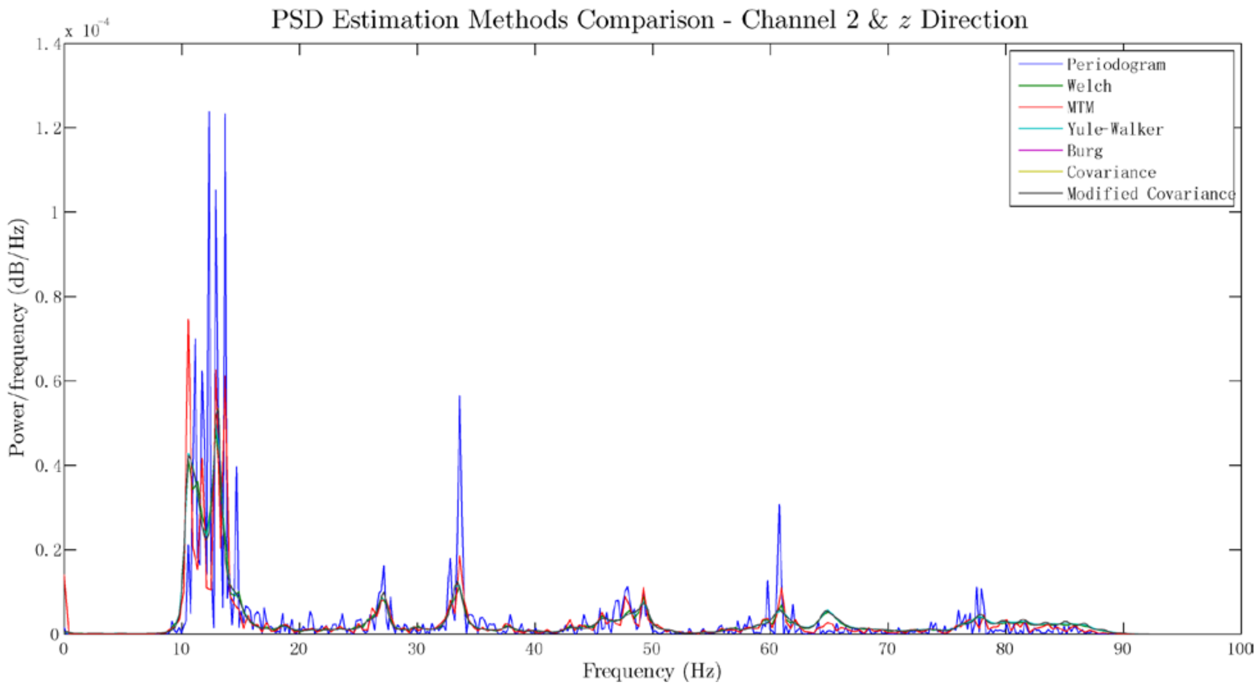

Figure 26. Comparison of PSD estimates for acceleration history of Channel 2 in z-direction.

It can be seen that these methods tend to yield peaks at consistent frequencies with some of them being more jagged than others. This is anticipated, because that they are all based on the Fourier transform but differ in terms of dealing with the estimation error. For the rest of the report, we will only discuss one method, i.e., the Welch's method with the default setting suggested in MATLAB Signal Processing Toolbox, that is, with 50% overlapping and the Hamming window.

4.4.3. Extracting Representative Frequencies: Normalized PSD

Figure 27 gives the PSD estimation of the entire preprocessed acceleration data of Test 134838 by using the Welch's method, where the power level of the z direction is about 100 times of those of either the x or the y directions. As outlined in Section 4.4.1, we are seeking the peak frequency values that are in common for the x, y, and z directions. For each direction, we have data from a total of four channels. Figure 27 in fact contains a total of twelve PSD results. This initially appeared as a sorting and clustering problem;

however, we cannot simply pick the frequency values following the rank of the power. This is because the forcing was in the vertical direction (i.e., z), which led to the most significant vibration and the most outstanding power of the PSD level - both in the vertical direction. Following the rank of the power would only make us miss the opportunity to study the forced response of the beam-slab system of the bridge span in x and y. This challenge calls for rational ways to compare the vibration in z with those in x and y that can be carried out consistently and systematically.

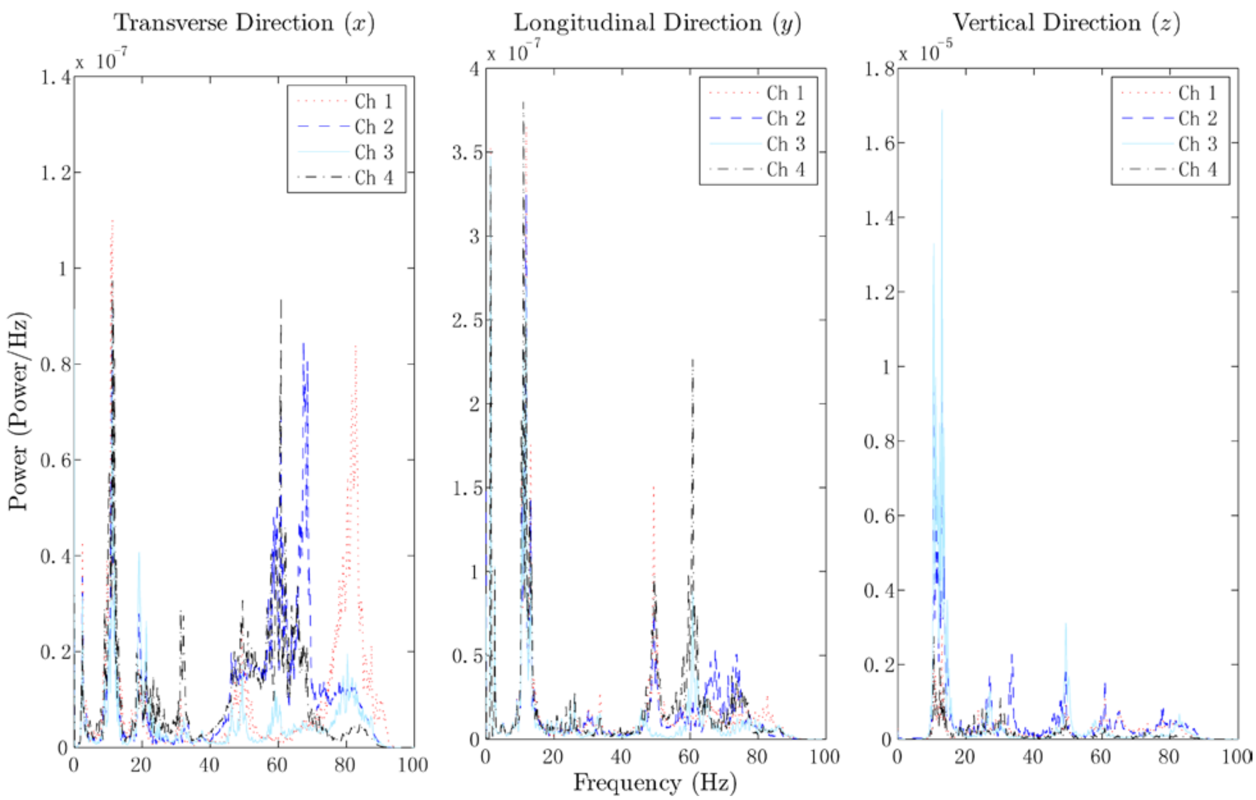

Figure 27. PSD estimation of the data in the three directions and from all four channels of Test 134838 by using the Welch's method.

Here we propose a so-called normalized PSD, abbreviated as NPSD, and apply it to each channel in each direction before extracting the frequencies of the peaks in power. The NPSD estimation is obtained by setting the maximum power value one in the PSD estimation for each channel along each direction. A NPSD plot is the same as its corresponding PSD plot except that an absolute power is replaced a relative power ranging from zero to one. The frequency of any peak in power is not altered, which serves the purpose. Normalized PSD has been used in the literature [19]; however, its meaning differs.

Figure 28 presents all NPSD plots for four channels and in three directions. In these 12 subplots in total, we further highlight the peaks with a relative power of not less than 20% for further consideration. This threshold is empirical as it leads to a proper resolution for the problem at hand.

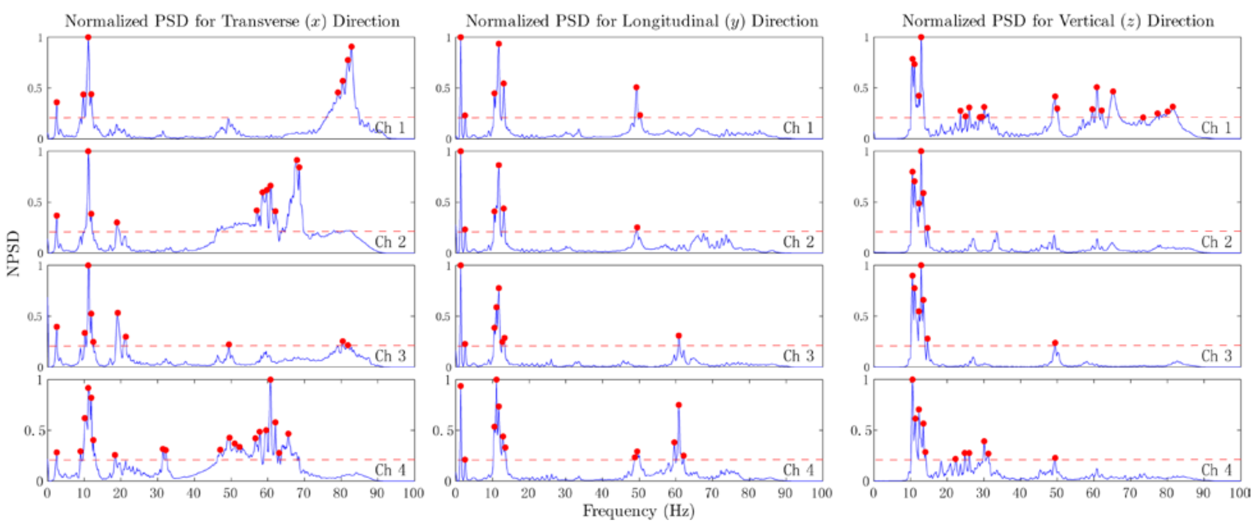

Figure 28. Normalized PSD estimation for four channels of Test 134838 in all three directions.

Table 9 lists the frequencies of the peaks in terms of relative power equal to or greater than 20% of all four channels in all three directions. We could continue with clustering techniques; however, we adopted an alternative path to condense the information in Table 9.

Table 9. Peak frequencies with their normalized power levels for Test 134838.

Channel	Transverse Direction (x)		Longitudinal Direction (y)		Vertical Direction (z)	
	Freq. (Hz)	Relative Power	Freq. (Hz)	Relative Power	Freq. (Hz)	Relative Power
1	**11.13**	1.00	**1.37**	1.00	12.89	1.00
	82.81	0.91	**11.72**	0.93	**10.55**	0.78
	81.84	0.77	13.09	0.54	11.13	0.73
	80.47	0.57	49.22	0.51	60.74	0.51
	79.10	0.46	10.55	0.45	65.23	0.46
	11.91	0.44	50.20	0.23	**12.30**	0.42
	9.77	0.44	**2.54**	0.23	49.41	0.42
	2.54	0.36			81.45	0.32
					30.08	0.31
					25.98	0.31
					50.00	0.30
					59.57	0.29
					62.11	0.28
					23.63	0.27
					80.08	0.27
					77.34	0.25
					25.00	0.22
					29.49	0.21
					28.91	0.21
					73.44	0.21
2	**11.13**	1.00	**1.37**	1.00	12.89	1.00
	67.97	0.91	**11.72**	0.86	**10.55**	0.80
	68.55	0.84	13.09	0.44	11.13	0.70
	60.74	0.66	**10.55**	0.41	13.48	0.59
	59.77	0.62	49.41	0.25	**12.30**	0.49
	58.59	0.60	**2.54**	0.23	14.65	0.24
	57.03	0.42				
	62.11	0.42				
	11.91	0.38				
	2.54	0.37				
	18.95	0.30				
3	**11.13**	1.00	**1.37**	1.00	12.89	1.00
	19.14	0.53	**11.72**	0.78	**10.55**	0.90
	11.91	0.52	11.13	0.59	11.13	0.77
	2.54	0.40	**10.55**	0.39	13.48	0.66
	10.16	0.34	60.74	0.31	**12.30**	0.55
	21.29	0.30	13.28	0.29	14.65	0.28
	80.47	0.25	12.70	0.25	49.41	0.24
	12.50	0.25	**2.54**	0.23		
	49.41	0.22				
	81.84	0.21				
4	60.74	1.00	11.13	1.00	**10.55**	1.00
	11.13	0.92	**1.37**	0.94	**12.30**	0.70
	11.91	0.82	60.74	0.75	11.33	0.61
	10.16	0.62	**11.72**	0.74	13.48	0.56
	62.11	0.58	**10.55**	0.54	30.08	0.39
	59.57	0.50	12.89	0.44	14.06	0.29
	57.81	0.49	59.57	0.38	24.80	0.28
	65.63	0.47	13.48	0.33	25.98	0.28
	49.61	0.43	49.41	0.29	31.25	0.27
	56.64	0.42	62.11	0.25	49.41	0.23
	12.50	0.41	48.83	0.23	22.27	0.22
	50.98	0.37	**2.54**	0.21		
	52.34	0.34				
	31.45	0.32				
	47.07	0.31				
	32.23	0.30				
	8.98	0.29				
	2.54	0.28				
	63.09	0.28				
	18.36	0.26				

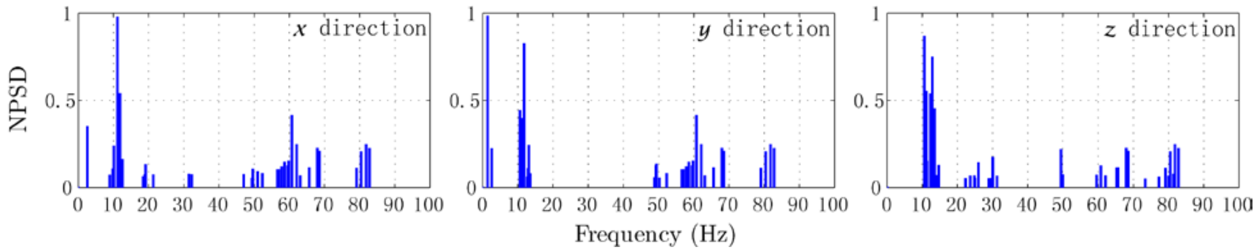

Figure 29. Consolidated NPSD estimation for each of the three directions in Test 134838.

With the following empirical guidelines, we continue to extract the most significant pieces of information:

- We treat each direction separately.
- We pay particular attention to the low-frequency vibrations in the transverse direction as well as those in the longitudinal direction.
- Within each direction, we assign the four channels with equal weight. The NPSD values are added up for all four channels and then divided by four. The added-up results in each direction are presented as one consolidated NPSD plot in Figure 29.

  Within each direction, the peak frequencies in common for all four channels are listed as follows:

  x**:** 2.54 Hz, 11.13 Hz, 11.91

  y**:** 1.37 Hz, 2.54 Hz, 10.55 Hz, and 11.72 Hz

  z**:** 10.55 Hz, and 12.30 Hz
- Now we utilize Figure 29 to identify the peak frequencies in common for all three directions. This could be done automatically using proper clustering techniques; however, we did it manually and found the following:
  - The narrow frequency band from 10.55 to 12.30 Hz marks the range for the fundamental frequency because the band is valid for all three directions. A range rather than a collection of discrete values is specified given the influence from the window length to the PSD estimation.

- The clusterings around 49.41 Hz and 60.74 Hz, respectively, are possible for the higher modal frequencies as they are shared in all three directions.
- The clustering just beyond 80 Hz will not be discussed further given the frequency response of the Etna sensor (see Section 2.3).
- 1.37 Hz in y only and 2.54 Hz in both x and y only are not modal frequencies; however, they need to be investigated as significant characteristics in dynamic responses.

4.4.4. Extracting Representative Frequencies: Coherence Function

Coherence function is used in modal analysis applied to input and output signals [19]. The idea of utilizing coherence function is that it tends to peak at the natural frequencies, as the signal-to-noise ratio (SNR) is maximized at these frequencies [20]. No cross-direction coherence functions were calculated.

Here we exercise the combination of every two output signals and use the high value in the coherence function to validate those frequency candidates from the previous section. The coherence values for two data sets were conveniently computed using the MATLAB built-in function mscohere, which estimates the magnitude square coherence (MSC) of two signals using the Welch's averaged modified periodogram method. The estimated coherence for three directions for all of the four channels is shown in Figure 30.

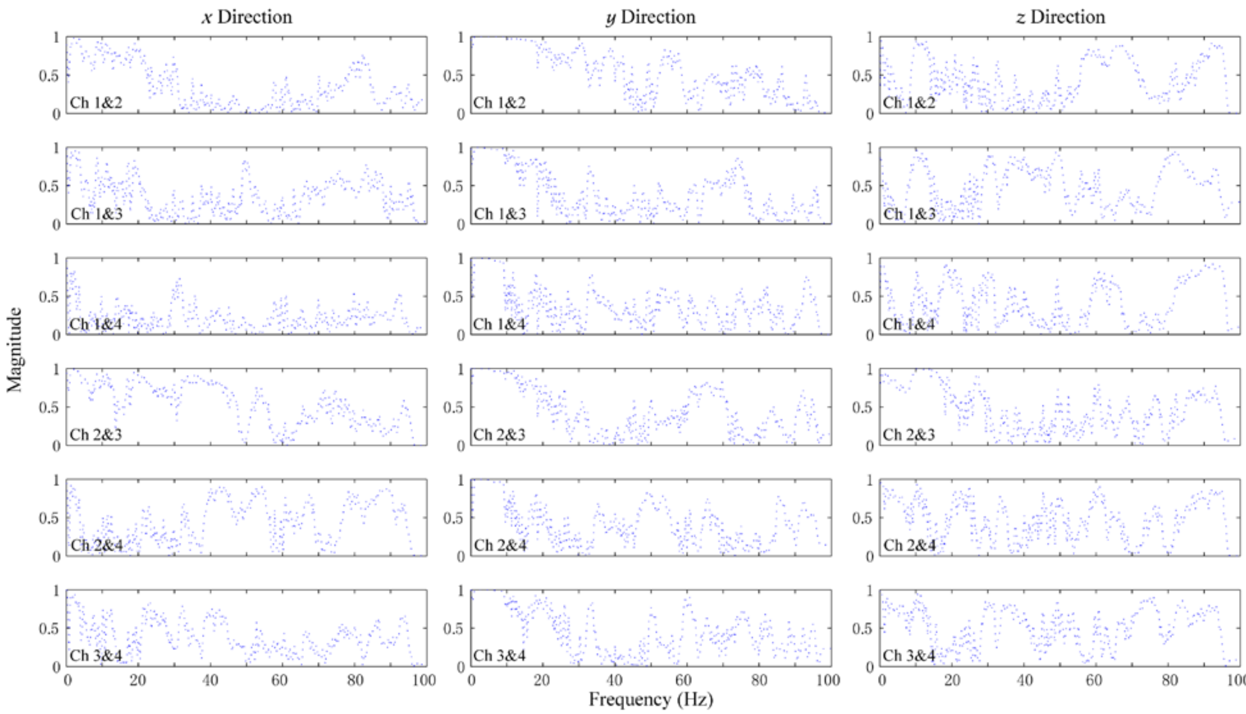

Figure 30. Estimated coherence functions between all four channels within each direction.

To carefully examine those frequency candidates, zoomed-in views of the coherence estimation plots were produced. Samples are given in Figure 31. The observations made in Section 4.4.3 are updated as follows:

- In z, the coherence values are greater than 0.7 at both 10.55 Hz and 12.89 Hz supporting the need for the fundamental modal frequency to fall within the range, although further zooming in to locate the specific value may be difficult.
- The coherence values around 49.41 Hz and 60.74 Hz, respectively, are not sufficient for us to decide if they are modal frequencies.
- 1.37 Hz in y corresponds to a coherence value of one for all six pairs of combinations supporting the claim to further investigate this significant dynamic characteristic. 2.54 Hz in x and y corresponds to the coherence values of greater than 0.7 and close to one, respectively, confirming the need to rule out this significant dynamic characteristic.

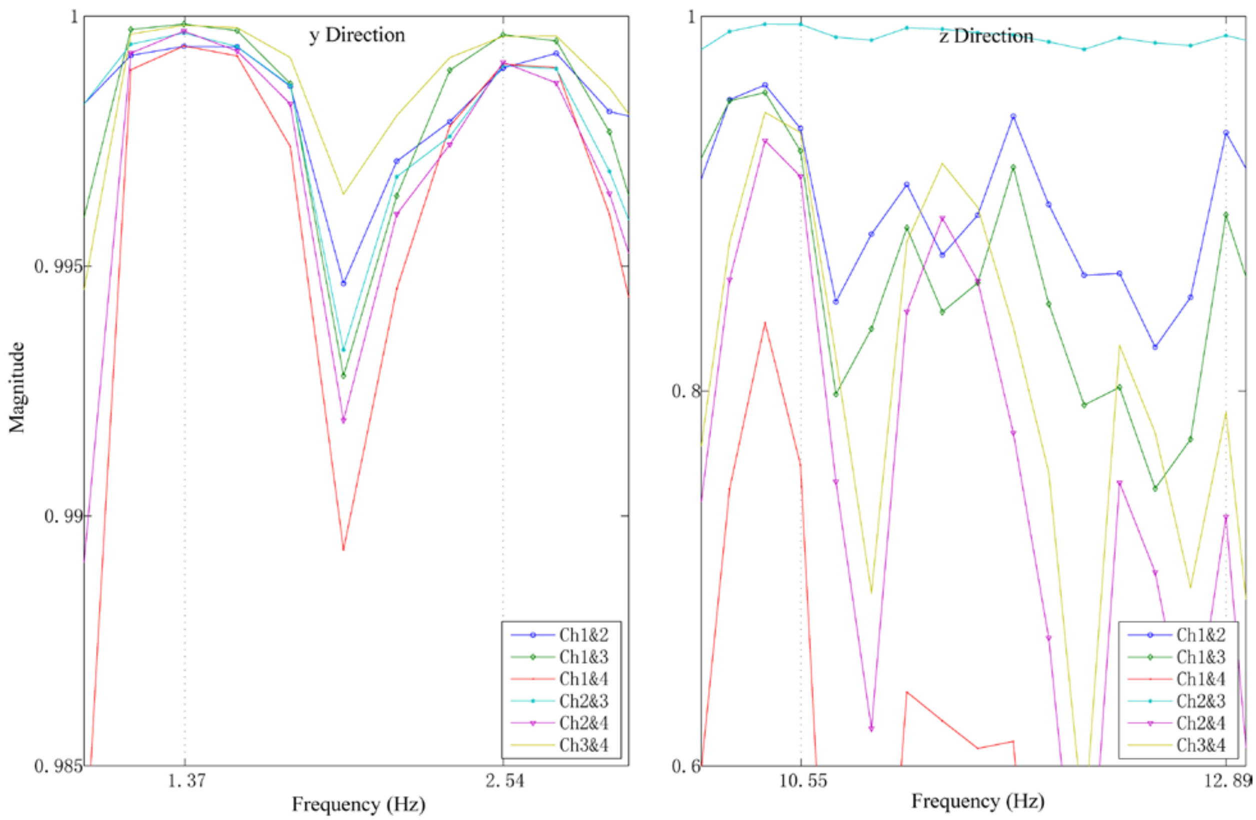

Figure 31. Samples of the estimated coherence functions for all four channels in certain directions.

4.4.5. Relative Motions - Elastic Deformations

The relative motions at mid-span and one-third span are analyzed using the Etna data from all except Test 150504, which was performed on multiple spans. NPSD was estimated similarly as before, but this time for the relative motion. As shown in Figures 32 and 33, at the mid-span, the two low frequencies completely disappear. At the one-third span, we can hardly see a hint of the two low frequencies. These observations indicate the need to look beyond the monolithic beam-slab superstructure for the reasons behind these two low frequencies.

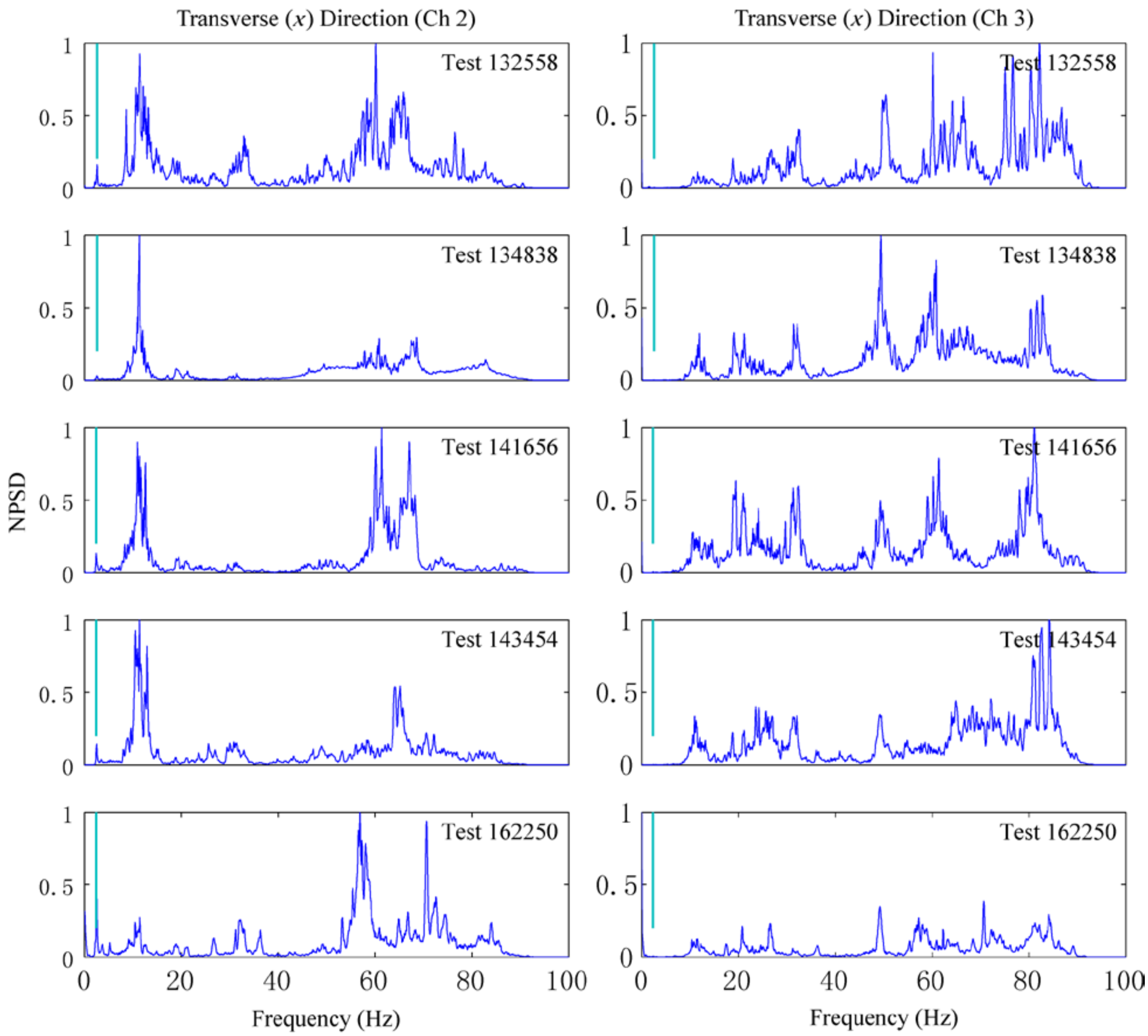

Figure 32. NPSD estimations for relative transverse motion. The vertical dash lines represent the locations of low frequency peaks for absolute motion.

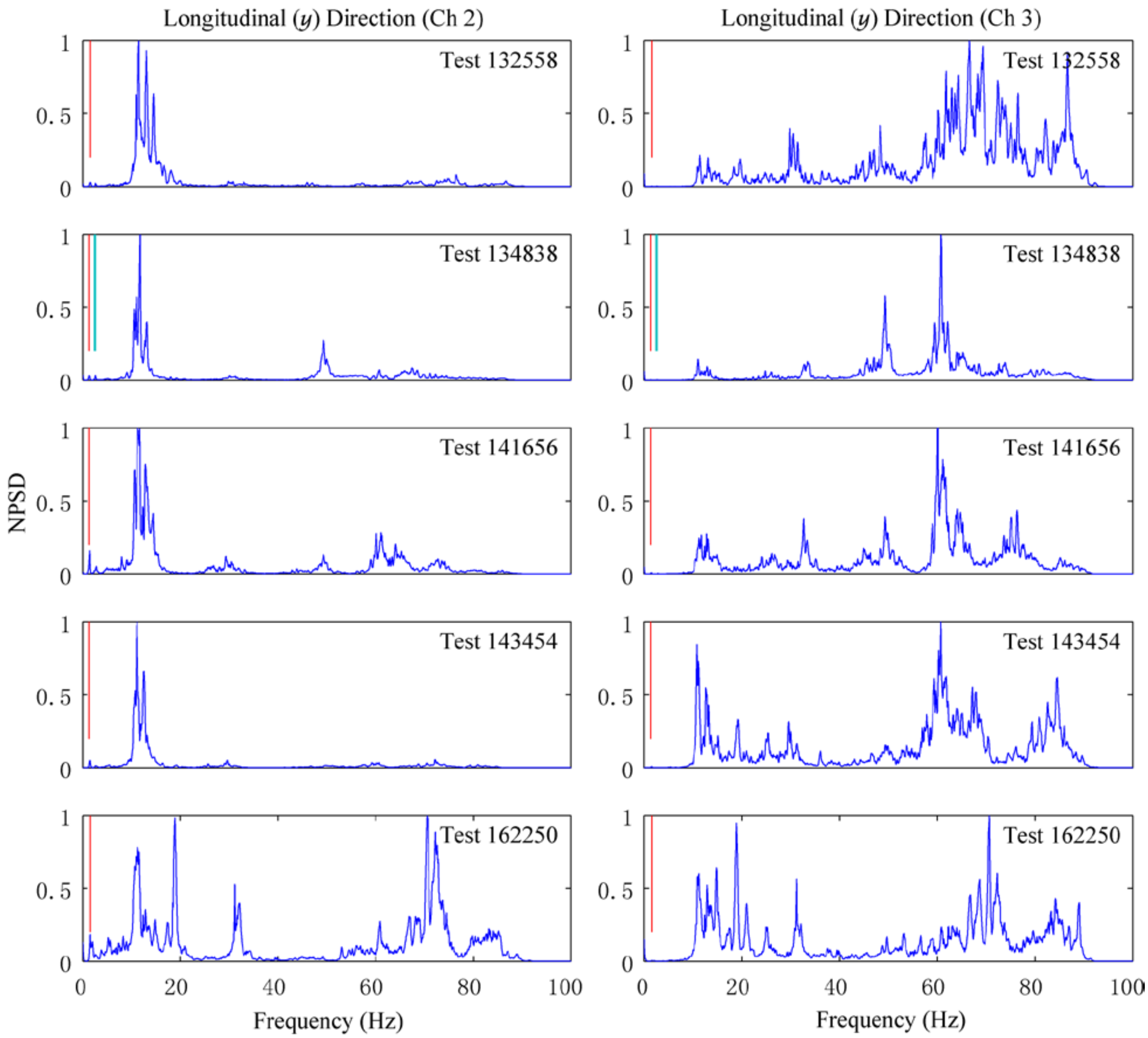

Figure 33. NPSD estimations for relative longitudinal motion. The vertical dash lines represent the locations of low frequency peaks for absolute motion.

4.4.6. Understanding Impact of Nonstationarity

Continuing with what has been mentioned previously, we evaluate the impact of nonstationary nature of the data to the result by estimating the PSD using the Welch's method to presentative pieces of an entire time history. Taking Test 134838 as an example, nine such pieces were selected, as shown in Figs 18 to 20, and processed; sample results are presented in Figure 34.

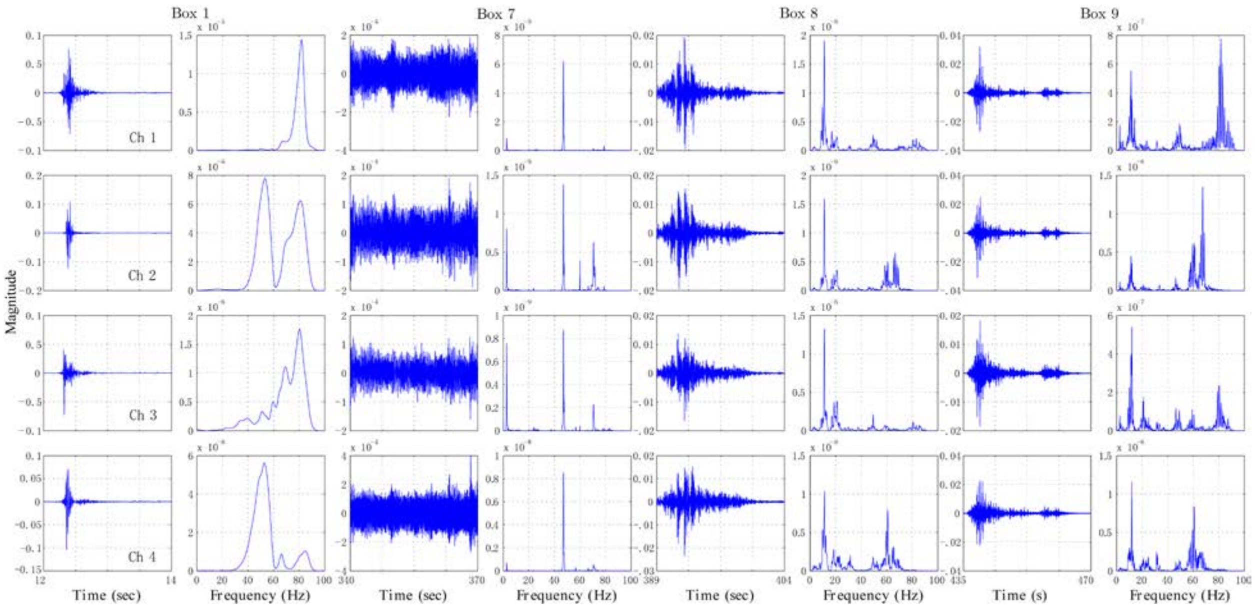

Figure 34. Sample results from the so-called piecewise analysis for Boxes 1, 7, 8 and 9 in x.

It can be seen that:

- Box 1 captures the moment of a hammer impact. Contrasting Box 1 with other boxes, it can be seen that the hammer impact causes the widest spread-out response spectrum.
- Boxes 2, 4, 6 and 7 correspond to restful or uneventful periods in the testing. It can be seen from them that (i) 2.54 Hz in x almost always exists in all channels even when no vehicles drive on the bridge, and (ii) 1.37 Hz and 2.54 Hz in y almost always disappear in all channels when no vehicles are on the bridge. In addition, from time to time, isolated peaks approximately at 50, 60 or 70 Hz can be observed at some channels in both x and y.
- Box 3, 5, 8 and 9 may be caused by one or multiple large vehicle(s) driving over the bridge span. The frequency band associated with the fundamental modal frequency almost always clearly displays at all channels in both x and y. Peaks

approximately at 20 Hz, 50 Hz, 60 Hz and beyond are observed from time to time in both x and y.

4.4.7. Comparison of Etna and SD Data

There are two data sets coming from Etna and SD sensors that were collected during the same period of time, from 13:26 to 13:38 pm. Therefore, we can make comparisons between these two data sets to further our understanding of the bridge vibrations. The difference between these two sets of data has been discussed previously in Section 3.2. The NPSD estimations for the two supports are plotted together and shown in Figures 35 and 36, and the NPSD estimations for the absolute and relative motion at one-third span are given in Figure 37 and 38, respectively.

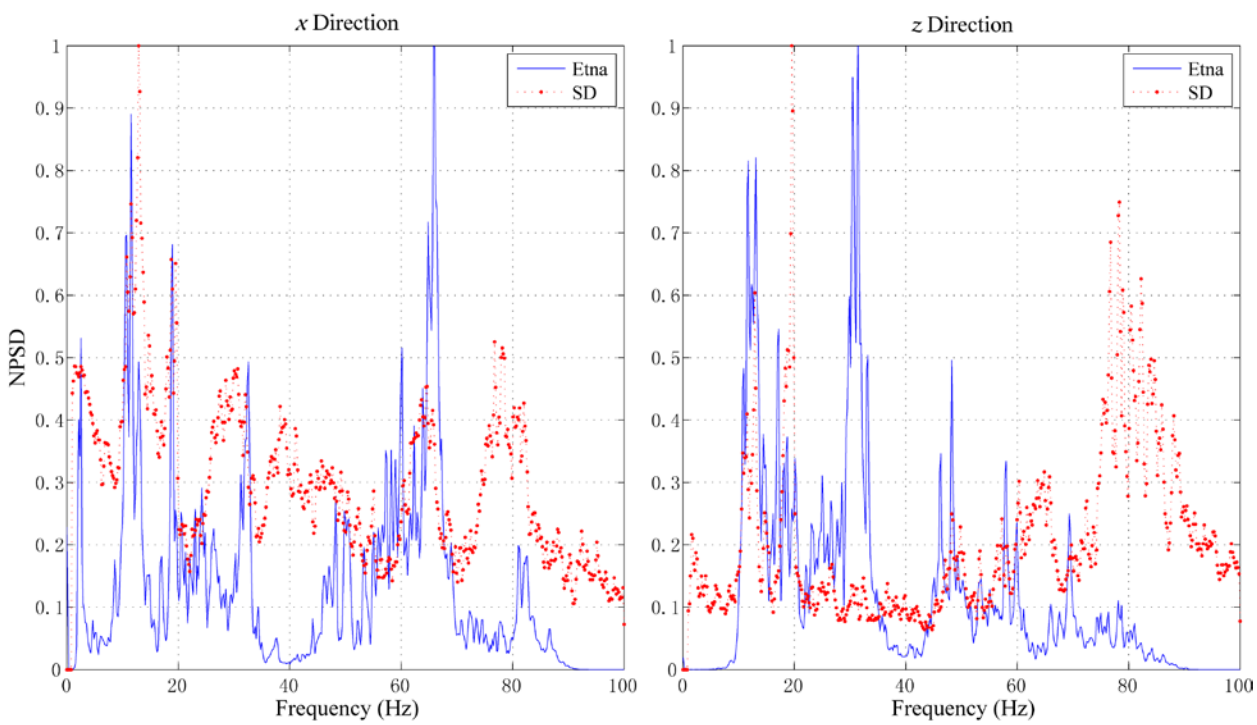

Figure 35. Comparison of NPSD of absolute motion at the south support.

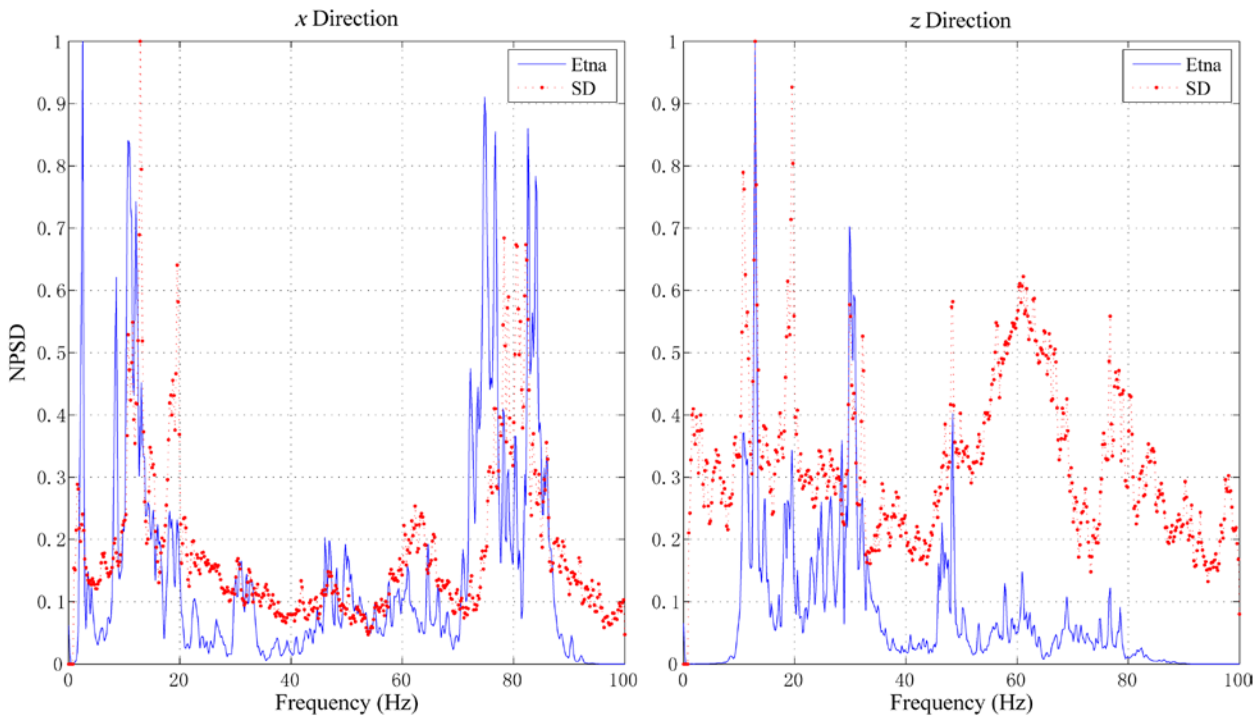

Figure 36. Comparison of NPSD of absolute motion at the north support.

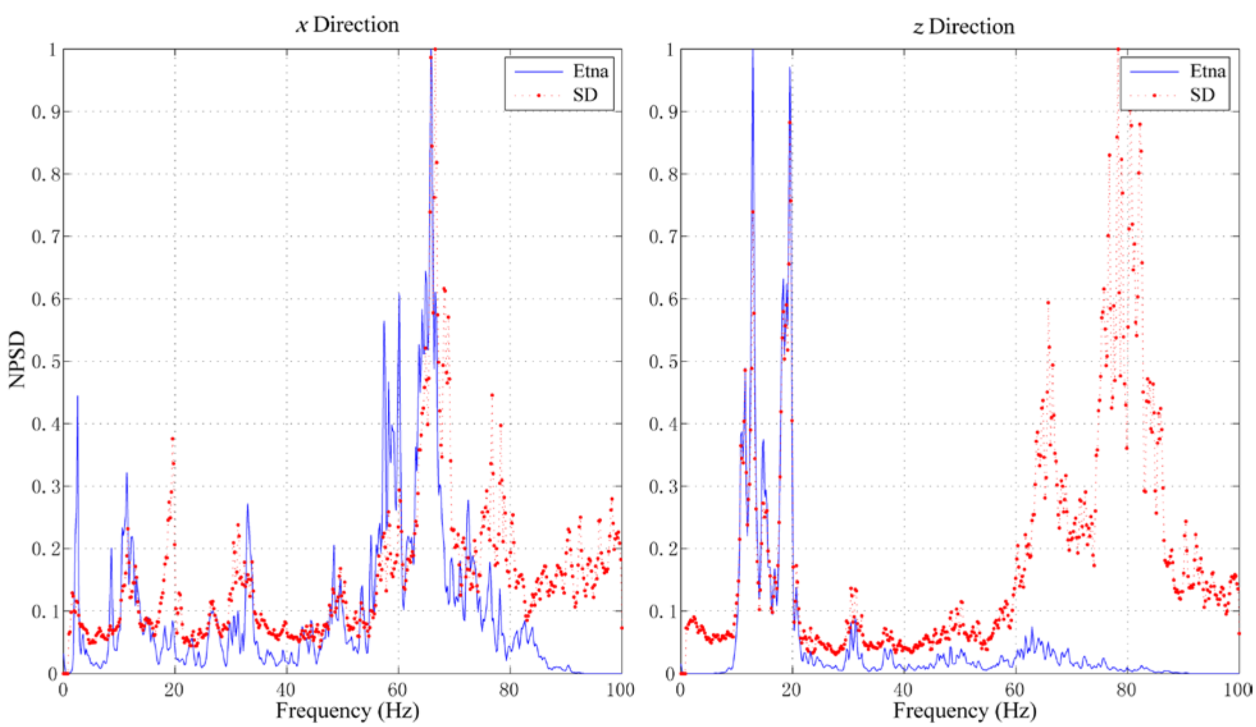

Figure 37. Comparison of NPSD of absolute motion at one-third span.

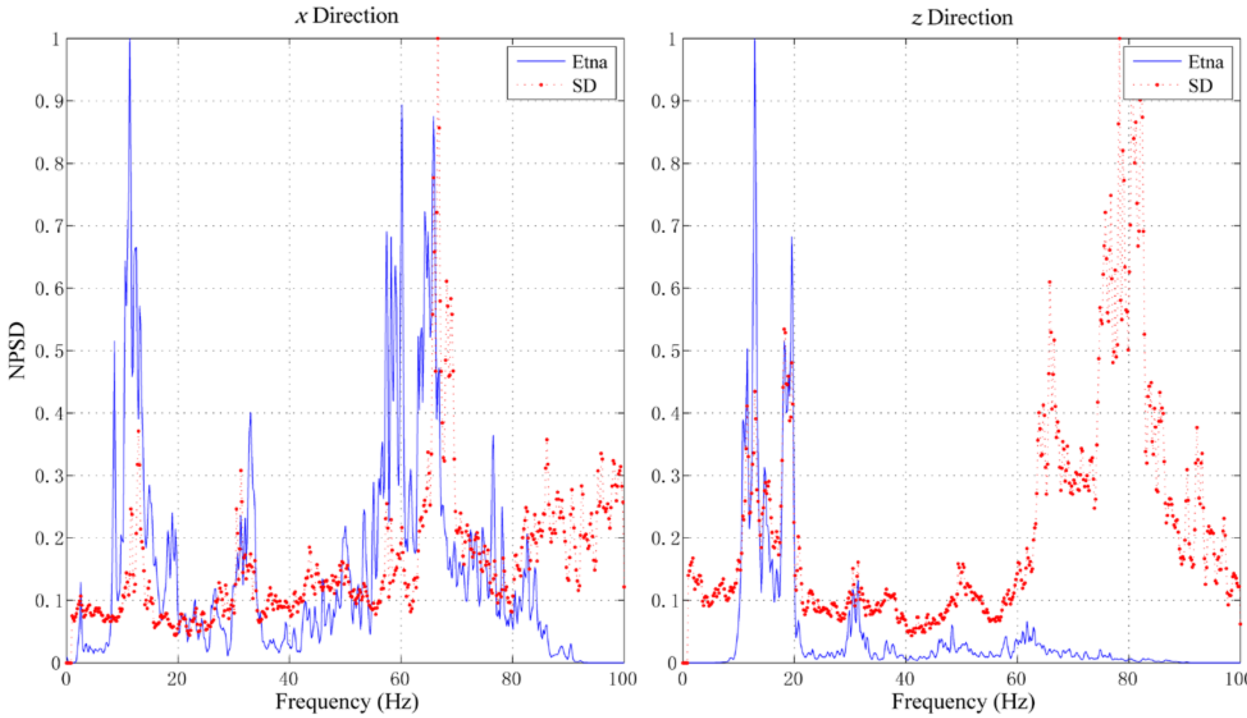

Figure 38. Comparison of NPSD of relative motion at one-third span.

Our observations are as follows:

- For the vibration in the transverse direction, overall Etna is quite consistent with SD, except the high noise floor with SD. In addition, the 2.54 Hz in x is confirmed using SD.
  - **At the south support:** Both Etna and SD data have obvious peaks at 11.52 Hz and 12.89 Hz. Other peaks are 18.95 Hz and 18.75 for Etna and SD, respectively. Etna has a significant peak at 65.82 Hz, which can be seen in SD but not as obviously. Also, Etna has a significant peak at 2.54 Hz, which shows in SD at approximately 2.54 Hz.
  - **At the north support:** While Etna has peaks at 10.74 Hz and 12.11 Hz, SD has a significant peak at 12.89 Hz and 19.53 Hz. Both Etna and SD have a peak in the range of 75 to 85 Hz and at 2.54 Hz.
  - **At the one-third span:** Etna and SD share a peak at approximately 11 Hz and 66 Hz. While Etna contains peaks around 60 Hz, SD peaks at

approximately 20 Hz and 80 Hz. Etna has a significant peak at 2.54 Hz, but SD's peak at the same frequency is not as significant.

- For the vibration in the vertical direction, overall Etna is quite consistent with SD up to approximately 60 Hz. There is a high noise floor with SD and additional peaks in frequencies beyond 60 Hz.
  - **At the south support:** While Etna has significant peaks at 11.52 Hz and 13.09 Hz, SD has them at 11.72 Hz and 12.89 Hz. However, Etna sees a significant peak at 31.45 Hz, while SD's is at 19.53 Hz.
  - **At the north support:** Etna and SD share two peaks at 10.74 Hz and 12.89 Hz. 19.53 Hz, 29.88 Hz, and 48.44 Hz are the other frequency values where Etna and SD share peaks.
  - **At the one-third span:** Etna and SD share significant peaks at 11.52 Hz, 12.89 Hz, and 19.53 Hz. While SD has significant peaks at approximately 68.52 Hz and 78.32 Hz, Etna is quite flat at these two places.

The observations in the previous subsections can be updated as follows:

- The narrow frequency band from 10.74 to 13.09 Hz marks the range for the fundamental frequency, which is fairly consistent with the band observed in the previous subsection.
- The clusterings at several high frequencies possibly indicate higher modal frequencies.
- 2.54 Hz in x most likely exists in the girder as well, but is not as obvious as in the deck.

5. RESULT ANALYSIS

The peaks in the output spectrum have the modal frequencies that we are seeking, and also have other characteristics of the forcing function as well. To extract the model frequencies, result analysis plays a critical role in this study. In addition, the low frequency peaks in both transverse and longitudinal directions deserve a good understanding, especially if they are related to the bridge safety. In this section, we will largely rely on simplified hand analysis to comprehend the data processing results and pave the road for delicate analysis based on finite element modeling.

5.1. Overview of Result Analysis

Narrow frequency band for fundamental modal frequency explained:

We will consider only the vibration in z and use a simple beam to model the entire monolithic beam-slab structure.

2.54 Hz in x explained:

This has been a challenge in our analysis and prompted us to carry out quite extensive data processing in Section 4. Eventually, we realized the need to examine the flexibility of the bridge pile bent. By modeling the pile bent as a single-degree-of-freedom (SDOF) structure, we will estimate its natural frequency for comparison with 2.54 Hz from the data processing.

1.37 Hz in y explained:

Section 4.4.6 points out that the occurrence of 1.37 Hz is strongly correlated with traveling vehicle, we will analyze the time it takes for a vehicle to travel a typical bridge span considering its allowable or actual speed.

Consolidated PSD discussed:

NPSD results have been heavily used in Section 4, where the consolidated PSD played a significant role. A simplified explanation is made to reveal a different understanding of this quantity.

Quantifying low-frequency motions in both transverse and longitudinal directions:

We intend to bridge the gap between the measured dynamic quantities with those in structural engineering especially designed quantities.

2.54 Hz in x explained again:

Human perception is used to understand why 2.54 Hz in x was felt during the field testing causing all concerns thereafter.

5.2. Validation of Modal Frequencies in Vertical Motion using Simplified Beam Model

Figure 39 shows a simple beam model for either one girder or the monolithic beam-slab structural system of the bridge span.

Figure 39. A model of a simply-supported beam.

An existing formula to calculate the simple beam's modal frequencies is employed

$$\omega_n = (n\pi)^2 \sqrt{\frac{EI}{mL^3}} \tag{14}$$

where L is the span, E is the elasticity of modulus, I is the moment of inertia of the beam cross section, and m is the mass of the beam.

A girder was modeled first, where L = 36 ft, and we calculated I = 50,980 in^4. E was estimated using the empirical formula recommended by ACI [21], i.e., $E = 57000\sqrt{f_c} = 4{,}030{,}509$ psi, where f_c is the cylindrical compressive strength of the concrete and was chosen as 5000psi according to the design drawing of the Little River overflow bridge [22]. m is calculated as $m = \mathrm{W/g} = \mathrm{\rho AL/g} = 35.84$ lbf-sec^2/in, and ρ and A denote the unit of the material and the cross-sectional area, respectively.

Plugging in all values to Eq. (14), we have the following

$$\mathrm{\omega_n} = (3.14\mathrm{n})^2\sqrt{\frac{4030509 \times 50980}{35.84 \times (36 \times 12)^3}} = 83.14n^2\mathrm{rad/\,sec} \Rightarrow\ f_n = 13.23n^2\ \mathrm{Hz}$$

Without considering the diaphragms, the entire beam-slab system was modeled next. While L and E remain the same, I = 570,887 in^4 and m = 604.91lbf-sec^2/in. Plugging in all values to Eq. (14), we have the following

$$\mathrm{\omega_n} = (3.14\mathrm{n})^2\sqrt{\frac{4030509 \times 570887}{604.91 \times (36 \times 12)^3}} = 67.72n^2\mathrm{rad/\,sec} \Rightarrow\ f_n = 10.78n^2\ \mathrm{Hz}$$

The estimated values of the first three modal frequencies are summarized in Table 10.

Table 10. Estimated modal frequencies using a simple beam model.

Mode n	1	2	3
Modal Frequency (Hz): One Girder Only	13.23	52.92	119.07
Modal Frequency (Hz): Beam-Slab System	10.78	43.12	97.02

It can be seen that first the fundamental frequency of the modeled beam-slab system, 10.78 Hz, is close to the lower bound of the identified narrow frequency band for the fundamental frequency. Further considering the existence of the diaphragms and coupled beam-slab effect leading to an increased stiffness, we would anticipate the actual fundamental frequency to be higher than 10.78 Hz. Next, we compared the weight of the trailer used in the testing (see Table 3.1) with that of the entire monolithic beam-slab system: 17,200 lbf vs. 233,550 lbf and felt that the influence on the trailer to the identified fundamental frequency would not be significant. Our results of all Etna data support this assessment.

5.3. Validation of Low-Frequency Motion in Transverse Motion using Simplified SDOF Model

Section 4.4.5 concludes that, very likely, 2.54 Hz in x does not cause elastic deformation. Section 4.4.6 discovers that the occurrence of 2.54 Hz has little to do with traveling vehicles. Section 4.4.7 further confirms that both the girder and deck undergo the same motion. These lead us to examine the substructure of the bridge pile bent shown previously in Figure 4 where the steel pile is HP 12 × 53 and the brace, L 4 × 4 × 3/8”. By modeling the pile bend as a SDOF structure, we will estimate its natural frequency for comparison with 2.54 Hz from the data processing. This SDOF can be excited by wind or water (see Figure 40) but not necessarily the vehicle.

$$f_n = \frac{1}{2\pi}\sqrt{\frac{k}{m}}, \qquad \text{with } k \approx 5k_{\text{pile}} + \delta \times 2k_{\text{brace}} \tag{15}$$

where $\delta < 1$ needs to be determined, and $\mathrm{k_{pile}} = 12\mathrm{EI}/\mathrm{h}^3, \mathrm{k_{brace}} = \mathrm{EA}/\mathrm{l}, \mathrm{m} = 743.90$ lbf-sec^2/in. The length $\mathrm{h} = 15'$ would be the shortest length according to Figure 4 and needs to be refined as well. Taking $\delta = 0$, 0.25, 0.5, 0.75 and 1, we have $\mathrm{f_n}$ = 1.14, 2.10, 2.75, 3.27, and 3.71 Hz, respectively.

Figure 40. A picture taken from underneath Span 4 during the field testing, where we can observe the water table.

To complete this analysis, first we need to understand why 2.54 Hz is seen in y with a possible correlation with the driving vehicle. If the 2.54 Hz is indeed caused by the motion in x of the bridge pile bent, then any mismatch in the phase of two adjacent bridge bents could lead to the motion in y of the beam-deck system. Not serving as a rigorous analysis, we feel that a driving vehicle could possibly cause a mismatch in the phase of the motions in x from two adjacent bridge bents. We will further this analysis by examining the following questions:

1. How much is the maximum horizontal force that the top of the bridge bent is subject to?
2. Has this magnitude of a horizontal force been considered in the design of the piles?
3. Have much is the maximum horizontal displacement?

5.4. Validation of Low-Frequency Motion in Longitudinal Motion using Simplified Analysis

Section 4.4.5 concludes that, very likely, 1.37 Hz in y does not cause elastic deformation. Section 4.4.6 indicates a strong correlation between 1.37 Hz in y and the traveling vehicle(s). Vehicles arrive on the bridge in a random pattern while each vehicle causes a number of wheel loads; therefore, a hand analysis technique can only be a highly simplified precursor to any rigorous analysis of this problem, say, using proper stochastic process models and theories.

We reckon that the wheels of a traveling vehicle on a particular span generate a horizontal force (the reaction of which is the friction force to the wheels), i.e., along the longitudinal direction y, and only last whenever the vehicle is driving on the span. This duration can be estimated as follows:

$$T = \frac{L}{v} = \frac{36}{65 \times \frac{5280}{3600}} = 0.38\,sec$$

where v is the speed of the vehicle. We assumed 65 mph for this state highway considering that, during the field testing, one lane was closed. While more quantitative analysis needs to be carried out, a quick understanding can be built on modeling this friction force as a boxcar excitation (i.e., input) with a period of 0.38 sec. Its frequency would be:

$$f = \frac{1}{T} = 2.65 \text{ Hz}$$

which is not too close but consistent with 1.37 Hz. More importantly, the compound effect of multiple wheels of one vehicle and even multiple vehicles arriving at the bridge span in a random pattern needs to be studied and used to further validate 1.37 Hz in y.

To complete this analysis, we wish to study the interactions between the monolithic beam-slab system and construction joint material and supports. If 1.37 Hz in y indeed does not cause elastic deformation, then the entire monolithic beam-slab system would move horizontally (i.e., in y) in a rigid-body fashion, while the construction joints and supports act as springs between the beam-slab and pile cap. Many questions follow such as:

1. How much is the maximum horizontal force that construction joints and the supports are subject to together?
2. Have both the construction joint and support been designed to take this horizontal force within their elastic limit?
3. Have much is the maximum horizontal displacement?
4. How does the maximum horizontal displacement compare with the detailing of both the construction joint and support?

5.5. Discussion of Consolidated PSD using Simplified LTI System Model

Rewriting Eq. (2), we have the following:

$$Y(j\omega) = H(j\omega)X(j\omega)$$

As mentioned previously, we only have $Y(j\omega)$. For the four channels in the same direction, each has its own $H(j\omega)$. However, we may consider them sharing the same $X(j\omega)$. Our consolidated PSD explained in Section 4.4.3 may be considered yielding an averaged $H(j\omega)$ of the four $H(j\omega)$. Nonetheless, we only have $Y(j\omega)$. The influence of the forcing function still exists in the processed PSD.

5.6. Understanding Experimental Observation: Quantifying Lateral and Longitudinal Motions at Low Frequencies

In parallel to seeking the mechanism behind the observed 2.54 Hz in x and y and 1.37 Hz in y, we also tried to quantify these motions so as to further understand their implications and assess their impact to the bridge especially bridge safety. The corresponding displacements and equivalent forces were estimated so that they could be compared with the relevant quantities specified in the design of the bridge.

It is known to the ASCE system identification community that estimating the displacement based on a measured acceleration history would not be a trivial task [23]. Here we chose to apply a band-pass filter with a very narrow frequency band before applying the inverse Fourier transform. 2 to 3 Hz and 1 to 2 Hz were used for x and y, respectively. While a sample result is presented in Figure 41, a summary is given in Table 5.6.

The equivalent forces were estimated to be in the range of 607.7 to 934.9 lbf for x direction, and 677.8 to 2571.1 lbf for y direction, respectively.

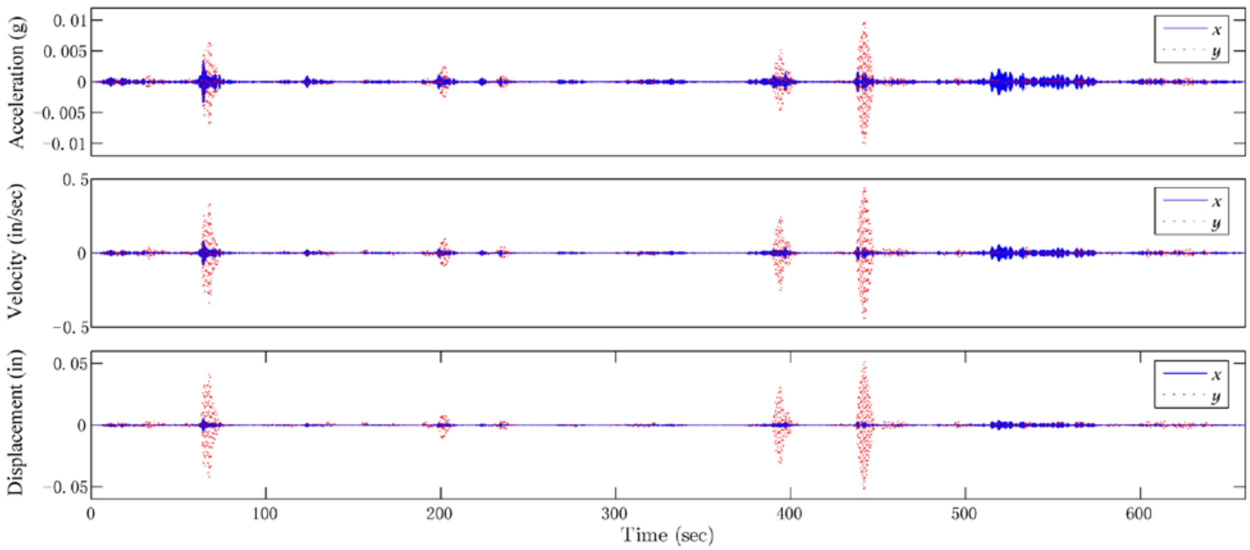

Figure 41. The filtered acceleration, estimated velocity and estimated displacement of 2.54 Hz in x and 1.37 Hz in y for Channel 4 of Test 134838.

Table 11. Amplitudes of the filtered acceleration, estimated velocity, estimated displacement of 2.54 Hz in x and 1.37 Hz in y for all but one Etna data sets.

Test ID	Channel	Transverse Direction (x)			Longitudinal Direction (y)		
		accel. (g)	velo. (in/s)	disp. (in)	accel. (g)	velo. (in/s)	disp. (in)
132558	1	0.0034	0.0893	0.0059	0.0086	0.3355	0.0337
	2	0.0030	0.0775	0.0050	0.0085	0.3340	0.0336
	3	0.0028	0.0706	0.0048	0.0085	0.3345	0.0337
	4	0.0029	0.0743	0.0048	0.0085	0.3349	0.0339
134838	1	**0.0040**	0.0969	0.0063	0.0103	0.4596	**0.0530**
	2	0.0037	0.0875	0.0058	0.0102	0.4577	0.0528
	3	0.0036	0.0839	0.0056	0.0103	0.4591	0.0528
	4	0.0034	0.0816	0.0052	0.0103	0.4589	0.0527
141656	1	0.0037	0.0895	0.0058	**0.0110**	0.4732	0.0527
	2	0.0035	0.0852	0.0054	0.0110	0.4716	0.0525
	3	0.0034	0.0832	0.0052	0.0110	0.4741	0.0528
	4	0.0032	0.0778	0.0051	0.0110	**0.4762**	0.0529
143454	1	0.0031	0.0711	0.0043	0.0071	0.274	0.0281
	2	0.0028	0.0633	0.0040	0.0070	0.2731	0.0280
	3	0.0026	0.0593	0.0038	0.0070	0.2739	0.0281
	4	0.0026	0.0629	0.0040	0.0070	0.2742	0.0282
162250	1	0.0038	**0.1002**	**0.0067**	0.0029	0.1212	0.0126
	2	0.0031	0.0786	0.0052	0.0029	0.1211	0.0126
	3	0.0030	0.0759	0.0050	0.0029	0.1216	0.0127
	4	0.0027	0.0734	0.0050	0.0029	0.1217	0.0127

5.7. Understanding Experimental Observation: Lateral Motion Perceived by Human

Discomfort of passengers and concerns about the bridge safety caused by lateral vibrations of high-pier bridges are reported [24]. In that study, the authors point out that “the lateral stiffness of high-pier bridges is usually small, and thus its lateral vibration can be produced easily by the moving vehicle loads and or wind loads.” There is a handful of work to study bridge lateral vibration induced by strong wind. In [24], a real-world seven-span two-lane continuous and straight concrete bridge in China was studied with 40 m in each span, 12 m in width, and 45 m of the highest pier. The structural system consists of five T-beams with 2.55 m in height and 28 transverse beams. The bridge’s lateral modal frequencies were measured as 1.987 Hz, 3.012 Hz, 3.756 Hz, 6.210 Hz, 8.436 Hz, while its vertical modal frequencies were measured as 3.663 Hz, 4.689 Hz, 6.010 Hz and 9.156 Hz.

The lateral motion of our structure indeed comes as a surprise since the bridge under study is not considered a high-pier bridge; however, the identified frequency 2.54 Hz in x appears consistent with the lateral modal frequencies in [24]. More importantly, our simplified analysis in Section 5.3 confirms our data processing result.

In [25], some general ideas are provided on human perception of vibrations. Without going through details and utilizing [25], a well-referenced paper in ergonomics and cited in [26]that presents experimental comfort contours for human beings subject to 0.5 to 5.0 Hz harmonic vibrations, we can tell that the frequency and amplitude of the measured vibrations in x in our field testing could possibly cause human discomfort. We also note that the human perception of vibrations can differ from individual to individual [26], which explains why not all team members felt the lateral motion of the bridge during the field trip.

6. OTHER WORK

6.1. Finite Element Modeling of Typical Span of Little River overflow bridge

We have obtained dynamic responses of a damped Mindlin plate model of a bridge deck. The main ideas are given as follows:

- The Mindlin plate model attempts to capture in-plane shearing behavior by assuming longitudinal and latitudinal displacements to be linearly z-dependent from the center plane located at z = 0.
- The material is assumed to be isotropic with elastic constants, Young's modulus and Poisson's ratio.
- The plate is assumed to be of uniform thickness. In plane displacements vary linearly with z while normal displacement is independent of thickness.
- Boundary conditions, either pinned or clamped, are imposed by penalization at x = 0 and $x = L$. The lateral boundaries are assumed to be free without conditions imposed.
- In this study the external forcing of the plate is by means of vehicles passing over the bridge. Using a plate model implies that surface forces arising from a vehicle are realized as body forces exerted on the plate. Hence, a vehicle is modeled as four point loads passing over the plate.
- A Mindlin model is applied to a bridge section in which the width is 45' and the length is 36' where two vehicles are supposed to traverse the bridge in opposite directions.

For prestressed concrete bridges, the values for the Poisson's ratio μ, density ρ, modulus of elasticity E_c may vary according to the actual material used, the prestressing force level, and the reinforcement ratio, and so on. Therefore, it is not practical to predict with accuracy the values of all of the above properties. Instead, we are trying to find a range for these parameters by referring to literatures.

Table 12 lists the suggested values or range of values for Poisson's ratio, material density and modulus of elasticity.

Table 12. The range for properties of materials according to literature.

Property	Suggested Value	Note	Reference
Poisson's ratio for concrete	0.11-0.21 2	lower for concrete of high strength	[27] [28]
concrete density (lb/ft^3)	135-160	normally taken as 145-150	[21]
modulus of elasticity for concrete (psi)	$57000\sqrt{f_c'}$	f_c' is the compressive strength, and is assumed to be 5000 psi in this study	[21]

6.2. Backbone Techniques

Developing comprehensive and high-fidelity models for nonlinear dynamical systems has been one of the key research issues in engineering mechanics (and beyond) impacting a very broad range of applications in civil, mechanical, aerospace engineering, and more. While there is very rich literature comprising theoretical, experimental and numerical work for a wide range of natural and engineered systems, substantial advancements in research and practice, however, are still in great demand. This is precisely the case for structural control, system identification, and SHM communities as summarized in, e.g., [29, 30, 31].

We explore insights to and possible connections among various ideas and methods named after "backbones" as appeared in the literature of nonlinear dynamical systems. To help with direct applications in nonlinear system identification, our goal is to achieve a unified understanding of these fundamental concepts and, if possible, to quantify different backbone characteristics for light-to-light comparisons. To launch this effort, we focus on the well-known Duffing equation for SDOF systems [32]. The improved understanding helps us derive improved approximated solutions to some backbone characteristics that are validated using numerical simulations.

In the traditional literature, a backbone arises from the frequency response function of a nonlinear SDOF system (e.g., [33, 34, 35, 36, 37]). The frequency response function is used to characterize the steady-state response under harmonic excitations, which can be obtained using the multiple-scale method, averaging method, or other methods equivalent to them. In particular, cusp bifurcation has been identified as the underlying geometry governing the well-known instability called "jump phenomenon" [38]. This backbone is nicknamed "traditional backbone" hereafter.

More recently, Michael Feldman [39, 40, 41, 42] has been developing techniques to extract backbones from both free and forced vibrations using analytic signals and the Hilbert Transform. A rich collection of prominent backbone patterns as well as the derived formulas in his work facilitate nonlinear system identification of these systems. This is because that the employment of the concepts of instantaneous amplitude and frequency of time history signals bridges the dynamic data (i.e., the time history signals) and the properties of the underlying system. These backbones are nicknamed "Feldman's backbones" hereafter.

It, however, remains unclear whether and how to connect "Feldman's backbones" with the more traditional backbone theory and patterns. This is our motivation from a theoretical viewpoint. At the same time, a number of simulation findings presented in Feldman's work remain unexplained and need further exploration. In our prior work to develop hardware-embedded algorithms for wireless structural health monitoring [43], we witnessed the need for more accurate mathematical derivations concerning one major type of the powerful Feldman's backbones. This is our motivation from a practical application viewpoint.

Using the Duffing equation, many backbones can be compared quantitatively through derivations rather than numerical simulations alone. The nature of the problems in terms of stability, the meaning of the variables (e.g., periodic solution vs. instantaneous characteristics), the assumptions made in multiple-scale and averaging methods versus those used in the analytic signal especially the Bedrosian identity can be carefully examined. These outline our effort to understand and unify the fundamentals.

To advance the existing body of knowledge, we pay particular attention to using a weighted sum of monocomponent signals, a general idea given in [42] for an approximated solution to the governing equation of motion, a 2nd-order nonlinear ordinary differential equation (ODE) in a particular format. Inspired by this general idea and limited to the Duffing equation in one loading condition, we leverage the harmonic balance method to derive a new formula for one basic type of Feldman's backbones that originally contains only one monocomponent [39]. Improved accuracy for the approximated solution to the Duffing equation is thus achieved. Numerical simulations validate this new formula and confirm the improvement. Our approach can potentially be generalized to other types of nonlinearities in a similar situation. The new formula introduces us new insights via a parametric study.

This study will enable us to better select or design dynamical experiments and greatly facilitate data processing and result analysis, thereby enriching the understanding of nonlinear phenomena in engineering mechanics applications especially for direct benefits in nonlinear system identification.

6.3. Inverse Problem

There are many challenging issues in inverse problem; here a snapshot is given to part of our literature review focusing on the bias/variance dilemma. We have been exploring the impact of model complexity to the identification result.

Table 13. Many faces of the bias/variance dilemma based on the triangle inequality.

Ref.	LHS	Term 1 in RHS +	Term 2 in RHS
[44]	$\| f - \hat{f}_{n,N} \| \leq$ total statistical risk	$\| f - f_n \|$ approximation error $\mathcal{O}\left(\frac{C_f}{n}\right)$ tends to zero with an increased n	$\| f_n - \hat{f}_{n,N} \| \leq$ estimation error $\mathcal{O}\left(\frac{nd}{N}\right) \log N$ tends to infinity with an increased n
[45]	$\mathcal{E}_D[(f(\vec{x};\ \mathcal{D}) - \mathcal{E}[y\|\vec{x}])^2] =$ “the average over the ensemble of possible $\mathcal{D}$”	$(\mathcal{E}_D[f(\vec{x};\ \mathcal{D})] - \mathcal{E}[y\|\vec{x}])^2$ bias model-based inference is bias-prone	$\mathcal{E}_D[(f(\vec{x};\ \mathcal{D}) - \mathcal{E}_D[f(\vec{x};\ \mathcal{D})])^2]$ Variance model-free inference is variance-prone
[46]	$\| R_\alpha y^\delta - x \| \leq$ the error b/w the exact and computed sol.	$\| R_\alpha y - x \|$ $= \| R_\alpha K x - x \|$ approximation error tends to zero with a reduced α	$\| R_\alpha y^\delta - R_\alpha y \|$ $= \delta \| R_\alpha \|$ the error in the data multiplied by the condition number tends to infinity with a reduced α
[47]	average generalized error	“due to insufficient model structure and an insufficient sample size"	"due to the fact that the function implemented by the network obtained on a specific data set deviates from the average function"

6.4. Markov Chain Monte Carlo Simulation

In addition to understanding the transitional Markov chain Monte Carlo (TMCMC) [48, 49]), programming the TMCMC algorithm was essential. It would be a straightforward process; however, a couple of implementation issues may directly affect the accuracy and efficiency of the code. According to [50], “there may be unspecified sub-algorithms such as computing finite difference approximations of Jacobians, iteration termination criteria, scaling and factorization, etc.” Therefore, a snapshot is provided here.

Table 14. Pseudo-code of what was developed during the project period following the transitional Markov chain Monte Carlo (TMCMC) [48, 49].

Detail #1 Sample from ln $\theta \in R$ rather than $\theta \in R^{+}$
Detail #2 Select prior PDFs
Declare global variables
Initialize "storage" for results / Start with log file

---

1. Sample from Prior PDFs
    Detail #3a Use of scaling factors to avoid ill-conditioning later in Step 4
    while $\beta < 1$, i.e., $i = 0 : M$

---

    2. Decide tempering parameter
        for $k = 1 : N$
        Call the developed *mymodel.m*
        Call the developed *loglikelihood.m*
        end - $k = 1 : N$
        Call the built-in *fsolve.m* to solve $\Delta\beta$ by setting c.o.v. = 1
        Call the developed *mybeta.m*
        Detail #4 Underflow/Overflow/Robustness problem
        Detail #5 Value for TolFun & initial values
    3. Obtain importance sampling weights
        Detail #4 Underflow/Overflow/Robustness problem

---

    4. Resample
        Calculate the mean vector and covariance matrix for MH per stage
        Detail #3b Use of scaling factors to avoid ill-conditioning
        for $dummy = 1 : N$
        Sample from multinomial distribution
        Detail #6 Call the built-in *mhsample.m*
        Call the developed *mhsample_logpdf.m*
        Call the developed *mymodel.m*
        Call the developed *loglikelihood.m*
        Detail #7 Use of joint lognormal for proposal PDFs
        Detail #8 Store results to avoid repetitive function evaluations in Step 2 at next stage
        Detail #9 Use burn-in in *mhsample.m*
        end - $dummy = 1 : N$

---

    end - while $\beta < 1$

7. CONCLUSIONS

Some acceleration time histories have been collected from the Little River overflow bridge primarily from representative locations on the bridge deck.

All data has been processed using both time- and frequency-domain analysis complemented with structural analysis using the first principle in mechanics and structural dynamics.

The fundamental frequency of the monolithic beam-slab superstructure is within the range of 10.55 to 12.30 Hz showing consistency with simplified hand analysis regarding the vibrations of a beam model.

The 2.54 Hz in the transverse direction of the bridge was felt by a very experienced team member during the field testing and has been identified in data processing. Our extensive analysis has been narrowed down to the natural frequency of the lateral vibration of the pile bent where five steel piles are oriented in their weak axis.

The 1.37 Hz in the longitudinal direction of the bridge has been identified in data processing. This frequency component seems to be caused by the forcing function of driving vehicle. Its implication to the bridge design is to be further examined.

8. RECOMMENDATIONS FOR FUTURE WORK

For field testing and instrumentation, a high-fidelity wireless sensor network is essential for collecting data underneath the deck. In addition to the girders, lateral motion of the bridge can be monitored with the change of the seasons. Together with system identification, the goal is to find out the capacity of the shear for the interior girders.

In 2010, Mr. Peng F. Tang searched the TRB database, BSI and Google before reaching the conclusion that BRUFEM does not support dynamic analysis. Given our current finding about the lateral motion of the bridge, exploring the capability of FB-MultiPier v4.18 or higher that can perform modal analysis would be rational for future work. The lateral motion of the bridge needs to be modeled in our in-house FEM model as well.

The backbone techniques and empirical mode decomposition (EMD) will be further developed leading to a systematic procedure of utilizing nonlinear dynamics to infer damages.

Model updating is needed for a typical span of the Little River overflow bridge with the goal of finding out the demand of the shear for the interior girders.

Our precious in-house test bed, a 26’-long real-world girder at OU Fears Lab should be thoroughly utilized in the development of our high-fidelity wireless sensor network, the nonlinear system identification technique and model updating. Only after the success of this step, more field testing would take place.

9. References

[1] S. Mitra, *Digital Signal Processing: A Computer-Based Approach*, 3rd ed. McGraw-Hill Companies, 2006.

[2] AASHTO Standard Specifications for Highway Bridges, 11th ed. AASHTO, 1973.

[3] LRFD Bridge Design Specifications. AASHTO, 2004.

[4] ASCE, "2009 report card for America's infrastructure," http://www.asce.org/reportcard, 2009.

[5] X. Yu and Y. Fu, "Dynamic analysis of damage behavior of vibration compaction on concrete bridges," in Traffic and Transportation Studies, Proceedings of the Seventh International Conference on Traffic and Transportation Studies, 2010.

[6] N. Bhkari, "Modal analysis of concrete bridge decks subjected to free vibration," Universiti Teknologi Malaysia, Tech. Rep., 2005.

[7] C. R. Farrar and G. H. James III, "System identification from ambient vibration measurements on a bridge," Journal of Sound and Vibration, vol. 205, no. 1, pp. 1–18, 1997.

[8] G. M. Lloyd, M. L. Wang, and V. Singh, "Observed variations of mode frequencies of a prestressed concrete bridge with temperature," in Condition Monitoring of Materials and Structures Proceedings of Sessions of Engineering Mechanics 2000, 2000.

[9] A. Morassi and S. Tonon, "Dynamic testing for structural identification of a bridge," Journal of Bridge Engineering, vol. 13, no. 6, pp. 573–585, 2008.

[10] O. S. Salawu and C. WIlliams, “Bridge assessment using forced-vibration testing,” Journal of Structural Engineering, vol. 121, no. 2, pp. 161–173, 1995.

[11] J. J. Carr, Sensor and Circuits: Sensors, Transducers, and Supporting Circuits for Electronic Instrumentation, Measurement, and Control. Prentice Hall, 1993.

[12] L. Ljung, System Identification: Theory for the User, 2nd ed. Prentice Hall, 1998.

[13] P. Welch, “The use of fast Fourier transform for the estimation of power spectra: A method based on time averaging over short, modified periodograms,” IEEE Transaction Audio Electroacoustics, vol. 15, pp. 70–73, 1967.

[14] L. D. Enochson and R. K. Otnes, *Programming and Analysis for Digital Time Series Data*. University of Michigan Library, 1968.

[15] MATLAB, *version 7.10.0 (R2010a)*. Natick, Massachusetts: The MathWorks Inc., 2010.

[16] MATLAB, “Comparison of different AR methods,” http://www.mathworks.com/help/toolbox/signal/f12-6587.html.

[17] D. J. Ewins, *Modal Testing: Theory, Practice and Application*, 2nd ed., ser. Mechanical Engineering Research Studies: Engineering Dynamics Series. Wiley, 2001.

[18] M. Aiello, A. Cataliotti, and S. Nuccio, “A comparison of spectrum estimation techniques for nonstationary signals in induction motor drive measurements,” *IEEE Transactions on Instrumentation and Measurement*, vol. 54, no. 6, pp. 2264–2271, December 2005.

[19] Y. Tsau and P. X. Chen, “Normalized power spectrum density function analysis on

spike trains i. mathematical method and its evaluation," *International Journal of Neuroscience*, vol. 49, pp. 115–121, 1989.

[20] G. M. L. Gladwell and A. Morassi, *Dynamical inverse problems: theory and application*. Springer Wien New York, 2011.

[21] A. C. ACI 318, "Building code requirements for structural concrete (ACI 318-08) and commentary," American Concrete Institute, Tech. Rep., 2008.

[22] *State of Oklahoma Department of Transportation, Plan of Proposed State Highway McCurtain County, Little River overflow bridge, Bridge D, Detail of Superstructure & Detail of P.C. Beam*, Oklahoma Department of Transportation, RF-40(53).

[23] A. W. Smyth and J. S. Pei, "Integration of measured response signals for nonlinear structural health monitoring," in *3rd US-Japan Workshop on Nonlinear System Identification and Health Monitoring*, Los Angeles, CA, 2000.

[24] X. Yin, Z. Fang, and C. Cai, "Lateral vibration of high-pier bridges under moving vehicle loads," *ASCE Journal of Bridge Engineering*, vol. 16, no. 3, pp. 400–412, 2011.

[25] C. Corbridge and M. Griffin, "Vibration and comfort: vertical and lateral motion in the range of 0.5 to 5.0 Hz," *Ergonomics*, vol. 29, no. 2, pp. 249–272, 2007.

[26] Mechanical vibration and shock - evaluation of human exposure to whole body vibration - Part I: general requirements, ISO 2631, Geneva, 1997.

[27] A. M. Neville, Hardened Concrete: Physical and Mechanical Aspects. American Concrete Institute, 1971.

[28] CP110, "British standards institution code of practice CP110: 1972 part 1, 'the

structural use of concrete’,” British Standards Institution, Tech. Rep., 1972.

[29] G. W. Housner, L. A. Bergman, T. K. Caughey, A. G. Chassiakos, R. O. Claus, S. F. Masri, R. E. Skelton, T. T. Soong, B. F. Spencer, and J. T. P. Yao, “Structural control: Past, present, and future,” Journal of Engineering Mechanics, special issue, vol. 123, no. 9, pp. 897–971, 1997.

[30] G. Kerschen, K. Worden, A. F. Vakakis, and J. C. Golinval, “Past, present and future of nonlinear system identification in structural dynamics,” Mechanical Systems and Signal Processing, vol. 20, no. 3, pp. 505–592, 2006.

[31] C. R. Farrar, K. Worden, M. D. Todd, G. Park, J. Nichols, D. E. Adams, M. T. Bement, and K. Fairnholt, “Nonlinear system identification for damage detection,” Los Alamos National Laboratory, Tech. Rep. LA-14353, 2007.

[32] K. I. and M. J. Brennan, The Duffing Equation. Wiley, 2011.

[33] J. J. Stoker, Nonlinear Vibrations in Mechanical and Electrical Systems. Interscience Publishers, 1961.

[34] J. Guckenheimer and P. Holmes, Nonlinear Oscillations, Dynamical Systems, and Bifurcations of Vector Fields, ser. Interdisciplinary Applied Mathematics Systems and Control, J. E. Marsden and L. Sirovich, Eds. New York: Springer, 1983, vol. 42.

[35] A. H. Nayfeh and D. T. Mook, Nonlinear Oscillations. Weinhein: Wiley-VCH, 2004.

[36] D. W. Jordan and P. Smith, Nonlinear Ordinary Differential Equations. Oxford University Press, 2007.

[37] T. Kalmár-Nagy and B. Balachandran, The Duffing Equation. Wiley, 2011, ch. Forced harmonic vibration of a Duffing oscillator with linear viscous damping, pp.

139–174.

[38] P. J. Holmes and D. A. Rand, “The bifurcations of Duffing’s equation: an application of catastrophe theory,” Journal of Sound and Vibration, vol. 44, no. 2, pp. 237–253, 1976.

[39] M. Feldman, “Non-linear system vibration analysis using Hilbert transform - i. free vibration analysis method ‘FREEVIB’,” Mechanical Systems and Signal Processing, vol. 8, no. 2, pp. 119–127, 1994.

[40] M. Feldman, “Non-linear system vibration analysis using Hilbert transform - ii. forced vibration analysis method ‘FORCEVIB’,” Mechanical Systems and Signal Processing, vol. 8, no. 3, pp. 309–318, 1994.

[41] M. Feldman, “Non-linear free vibration identification via the Hilbert transform,” Journal of Sound and Vibration, vol. 208, no. 3, pp. 475–489, 1997.

[42] M. Feldman, “Hilbert transform in vibration analysis,” Mechanical Systems and Signal Processing, vol. 25, pp. 735–802, 2011.

[43] J. D. Jones and J. S. Pei, “Embedded algorithms within an FPGA to classify nonlinear single-degree-of-freedom systems,” IEEE Sensors Journal, vol. 9, no. 11, pp. 1486–1493, November 2009, special Issue on Sensor Systems for Structural Health Monitoring.

[44] A. R. Barron, “Approximation and estimation bounds for artificial neural networks,” Machine Learning, vol. 14, pp. 115–133, 1994.

[45] S. Geman, E. Bienenstock, and R. Doursat, “Neural networks and the bias/variance dilemma,” Neural Computation, vol. 4, pp. 1–58, 1992.

[46] A. Kirsch, An Introduction to the Mathematical Theory of Inverse Problem, Applied Mathematical Sciences Series, Springer, 1996, vol. 120.

[47] M. Norgaard, O. Ravn, N. K. Poulsen, and L. K. Hansen, Neural Networks for Modelling and Control of Dynamic Systems: A Practitioner’s Handbook, ser. Advanced Textbooks in Control and Signal Processing Series, Springer, 2000.

[48] J. Ching and Y.-C. Chen, “Transitional Markov chain Monte Carlo method for Bayesian model updating, model class selection, and model averaging,” ASCE Journal of Engineering Mechanics, vol. 133, no. 7, pp. 816–832, 2007.

[49] M. M. Muto, “Application of stochastic simulation methods to system identification,” Ph.D. dissertation, California Institute of Technology, Pasadena, CA, 2006.

[50] G. Söderlind and L.Wang, “Adaptive time-stepping and computational stability,” Journal of Computational Methods in Science and Engineering, vol. 2, no. 3, pp. 1–19, 2003.